MANGANESE DIOXIDE REDUCTION KINETICS BY *GEOBACTER SULFURREDUCENS* AND ASSOCIATED BIOFILM MORPHOLOGY IN A FLOW-THROUGH REACTOR

BY

ERIN C. BERNS

THESIS

Submitted in partial fulfillment of the requirements
for the degree of Master of Science in Environmental Engineering in Civil Engineering
in the Graduate College of the
University of Illinois at Urbana-Champaign, 2015

Urbana, Illinois

Advisers:

Professor Albert J. Valocchi
Professor Charles J. Werth

ABSTRACT

In natural aquatic environments such as streams, lakes, and groundwater, microorganisms play an important role in the cycling of metals. Dissimilatory metal reducing bacteria (DMRBs) are a specific type of bacteria that convert metals to lower redox states through oxidation and reduction reactions. They utilize more metal than is needed for biosynthesis because they can conserve energy through the reduction of metals. This ability of DMRBs permits them to influence nutrient cycling in marine and lacustrine environments and control the bioremediation of sediments and waters contaminated with metals. Because of their widespread occurrence and impact on the environment, many kinetic models have been developed to evaluate fate and transport of metals in the presence of DMRBs. These models use various parameters to describe the reduction kinetics of DMRB and oftentimes rely on using parameters that are determined in batch systems.

Batch systems do not adequately account for the variation that may exist in kinetic parameters. They are unable to estimate how environmental conditions present in a flow-through system could impact the reduction efficiency of DMRBs. Some of these changes can be accounted for by incorporating more terms into the models, but others are still unable to be quantified in this manner. By exploring how these parameters change under different flow conditions and which ones are impacted the most, we can determine where more work is needed to identify the actual mechanisms that cause differences in parameters. Additionally, batch systems are less useful for estimating kinetic parameters when DMRBs are reducing a solid substrate. This is because estimates of biomass in a biofilm on a solid surface are more difficult to obtain than measuring the cells in solution when a soluble phase substrate is utilized in a batch system.

In this study, a flow through system with a solid phase electron acceptor is used to quantify important kinetic parameters at different flow rates. The biomass is estimated using a unique approach that involves coating sections of the reactor with the solid phase electron acceptor and removing these sections intermittently over the course of the experiment to evaluate both total biomass and biofilm morphology. We chose to explore the biofilm morphology throughout each experiment and at different flow rates in hopes of correlating morphology trends to reduction kinetics. A relationship between morphology and reduction kinetics could help explain differences in the parameters estimated from the experiments.

This study evaluated the reduction kinetics of manganese dioxide using *Geobacter sulfurreducens*, an extensively studied DMRB, with acetate as the electron donor. At low flow rates, a yield of $3.44 \times 10^{10} \pm$

$2.54x10^{10}$ cells/mmol MnO_2 was calculated and a maximum specific growth rate of 0.02 1/hr was estimated. The half saturation constant was fit with the model and determined to be 0.04 mmol MnO_2 for the low flow rate. When the experiment was conducted at higher flow rates, the half saturation constant was determined to be 0.01 mmol MnO_2, which indicates more efficient microorganisms. These findings show that higher flow rates, within the range evaluated in this study, may contribute to lower half saturation constants. The difference in half saturation constants may be related to changes in biofilm morphology, but more work needs to be done to conclusively make this comparison.

ACKNOWLEDGEMENTS

I would first like to thank my advisers, Dr. Albert Valocchi and Dr. Charles Werth, for committing their time and offering their expertise to assist me in this work. I cannot thank them enough for their patience through my various research efforts and thesis writing. I would also like to thank Dr. Robert Sanford for his willingness to share his expert opinion related to biogeochemical interactions and provide advice related to culturing of bacteria. I am especially grateful to Kyle Michelson for his assistance in the lab; he introduced me to many of the biological techniques necessary for this work and was always willing to share his insight and offer encouragement. I would also like to thank the other members of the Werth Research Group for their support and help in the laboratory.

Finally, I would like to thank my friends and family for being supportive of my graduate school pursuits and believing that I can have a positive impact on the world through my graduate research. I would like to especially thank my mother and my boyfriend for the many hours they spent listening to my frustrations and encouraging me.

TABLE OF CONTENTS

CHAPTER 1: INTRODUCTION AND BACKGROUND 1
CHAPTER 2: METHODOLOGY 5
2.1 Materials 5
2.2 Flow-Through Reactor Setup and Operation 6
2.3 Data Collection 8
2.4 Modeling Methods 10
CHAPTER 3: RESULTS 13
3.1 MnO_2 Reduction Kinetics 13
3.2 MnO_2 Reduction Mass Balance 14
3.3 Laser Confocal Imaging Results 17
3.4 Protein Assay results 20
3.5 Modeling Results 22
CHAPTER 4: DISCUSSION 27
CHAPTER 5: CONCLUSIONS AND FUTURE WORK 32
REFERENCES 34
APPENDIX A: LARGE TABLES 37
APPENDIX B: RAW DATA 39
APPENDIX C: CONFOCAL IMAGES AND IMAGE ANALYSIS 44
APPENDIX D: CALCULATIONS 50
APPENDIX E: MODEL OUTPUTS 53

CHAPTER 1: INTRODUCTION AND BACKGROUND

It is important to understand the coupled biogeochemical interactions occurring in aquatic sediments and groundwater because they influence both natural processes and the fate and transport of contaminants in the environment. Dissimilatory metal reduction, a process in which microorganisms transfer electrons to metals in their environments without assimilating the metals, plays an important role in these interactions (Lovley, 2013; 1993). Kinetic models have been developed to determine the influence of dissimilatory metal reducing bacteria (DMRB) on nutrient cycling in marine and lacustrine sediments, and to explore groundwater bioremediation efforts and monitored natural attenuation (Fang et al., 2009; Li et al., 2009; Liu et al., 2002; Truex et al., 1997; Yabusaki et al., 2007). The effectiveness of these models in predicting biogeochemical interactions is dependent on the quality of the kinetic and biological parameters used in the models. Because DMRBs often form as a biofilm in the natural environment, it is necessary to understand how environmental conditions may alter biofilm formation and function and potentially influence these important parameters. Various studies have noted the influence of hydrodynamic conditions on the growth rate, attachment, and morphology of biofilms (Costerton et al., 1995; Hall-Stoodley et al., 2004; Purevdorj et al., 2002). This study is specifically concerned with the impact of different flow rates on biofilm morphology and the parameters involved in reduction kinetics.

Dissimilatory metal reduction is a type of anaerobic respiration that differs from assimilative microbial processes that involve taking metals into the cell for biosynthesis. Assimilative metabolisms reduce only the amount of metal needed for cell processes and production of macromolecules, but dissimilative metabolisms will reduce more of the metal than necessary for biosynthesis and leave behind reduced metal products in order to conserve energy for cell growth (Madigan et al., 2010). Studies have shown that oxidation of organic matter coupled to metal reduction can yield energy for microbial growth (Lovley & Phillips, 1988). Dissimilatory metal reduction is important for understanding the origin of microorganisms on earth, modern biogeochemical cycles, and bioremediation of contaminants (Lovley, 2002).

Many different metals can be involved in dissimilatory metal reduction including, but not limited to, iron, manganese, uranium, selenium, chromium, and mercury, as well as the lesser studied technetium, vanadium, molybdenum, gold, silver, and copper (Istok et al., 2004; Liu et al., 2002; Lovley, 1993). Iron, which undergoes dissimilatory metal reduction, is arguably the most important metal in the environment because of its role in many biogeochemical cycles (Lovley, 2013; Lovley, 1993; Tebo et al.,

2004). Uranium is another metal that is well studied due to its persistence in the environment following the Cold War Era. (Anderson et al., 2003; L. Li et al., 2009; Williams et al., 2007; Wu et al., 2006; Yabusaki et al., 2007; Zhong et al., 2005). Uranium can be reduced by DMRB and most literature focuses on the importance of dissimilatory metal reduction in remediation of contaminated sites. Manganese can also be used by DMRB, and is a metal found naturally in the environment in minerals such as birnessite, todorokite, and other metal oxides (Post, 1999). It can exist in a wide range of oxidation states from Mn(II) to Mn(VII), and plays an important role as an electron carrier in biogeochemical cycling in marine and lacustrine settings as well as groundwater systems. More recently, in some parts of the world, manganese has been studied as a groundwater contaminant because of its high concentrations in some surface and groundwater environments (Homoncik et al., 2010; Li et al., 2013).

Due to the complexity of the electron transport system within the DMRB cell membrane, models often use macroscopic approaches to evaluate the kinetics involved in dissimilatory metal reduction (Liu et al., 2002). Monod kinetics has historically been used to model substrate utilization and biomass growth, and depends on the cell yield, the maximum specific growth rate, a half saturation constant, biomass concentration, and the concentrations (or masses) of the electron donor and acceptor. Typical modeling efforts evaluate a system using some experimentally derived parameters, and if all of the parameters needed are not available, experiments are conducted and the model is used to fit the experimental data to determine the other parameters necessary. For example Liu et al. used the Monod expression to simulate the reduction of a group of polyvalent metals by four different DMRB and assumed constant biomass to limit the model to two unknown parameters (2002). Because there were only two unknowns, these parameters were adjusted to fit experimental data.

There are challenges using Monod kinetics. In some cases, the biomass is assumed to be constant. However, biomass grows and decays in many systems and this adds a level of complexity to Monod kinetics. Biofilms make determining the amount of biomass especially difficult because they contain extracellular polymeric substances in addition to microbial cells. It is also difficult to evaluate Monod kinetics when solid phase electron acceptors are involved because most parameters for Monod kinetics are determined in batch reactors with soluble electron donors and acceptors.

In this study, we look at incorporating biomass growth and the impact of solid phase electron acceptors into our analysis of reduction in a flow-through system. When biomass growth is evaluated in a well-controlled batch reactor with soluble electron donors, where thick biofilms are not dominant, it is possible to determine the biomass concentrations using optical density. This is not possible when thick biofilms grow on the surface of a solid phase electron acceptor, so other methods to estimate biomass

are needed. Additionally, parameters such as yield, maximum specific growth rate, and half saturation constant are dependent on these estimates of biomass (Brown et al., 2005; Holmes et al., 2013; Liu et al., 2002). In order to explore how these parameters vary in a flow through system, it is imperative to estimate the actual biomass growing on a solid surface.

Biofilm growth and reduction kinetics are influenced by a variety of environmental conditions. Nutrient transport can impact the morphology of a biofilm. According to Picioreanu et al., biofilms are more compact when nutrients are available and tend to form more irregular surfaces when nutrients are limited (2000). The surface area of a solid phase electron acceptor impacts reduction kinetics. For example, experiments with iron oxides have shown that the surface area of the oxide has a greater impact on the initial rates of reduction than thermodynamics (Roden, 2006; Roden & Zachara, 1996). Interactions between bacteria also impact biological reduction. Bethke et al. conducted a very detailed analysis of the different reduction zones in the subsurface and found that the different redox zones in the subsurface are dominated by different bacteria, and that this relationship is not solely controlled by thermodynamics - population viability and mutualism have an equally important impact on microbial reduction processes in the subsurface (2011). Holtan-Hartwig et al. looked at different nitrifying bacterial communities and concluded that the reduction parameters were different for different communities at the beginning of the experiments (2000).

Water flow rate also affects biofilm morphologies, and subsequently kinetic parameters. It has been shown to impact biofilm morphology through its effect on the rate of reattachment of cells, biofilm density, and biofilm structural integrity (Korber et al., 1989; Stoodley et al., 2002). Less reattachment or stronger biofilms could impact the effective biomass yield and ultimately influence reduction of the electron acceptor. Stronger, more cohesive biofilms may also be more efficient at transporting electrons. These physical mechanisms may manifest themselves as differences in kinetic parameters between high and low flow rates.

The goal of this study is to determine the effect of variable flow conditions on biofilm morphology and the associated reduction kinetics of manganese dioxide using *Geobacter sulfurreducens* as a model metal-reducing bacteria. The first objective of this work is to determine differences in reduction kinetics at two different flow rates by estimating microbial yield, maximum specific growth rate, and the half saturation constant from experimental data. The second objective is to determine if differences in kinetics at different flow rates are related to biofilm morphologies. Based on the limited body of literature available, we hypothesize that slower flow rates will result in biofilms with more structure such as mushroom shapes and towers and that higher flow rates will limit the biofilm morphology to thin film

structures. We also hypothesize that the more complex biofilm structure will lead to slower reduction of the MnO_2 because its less dense morphology will limit the transport of electrons through the biofilm and make it more prone to biomass detachment.

These hypotheses were tested using a simple flow-through reactor with removable glass slides coated in manganese dioxide (MnO_2) to facilitate biological reduction of solid-phase MnO_2 with acetate as the electron donor. Acetate (CH_3COO^-) was chosen as the electron donor because it is a simple organic molecule that is a common reaction product of the fermentation of more complex organic molecules, and it can be oxidized directly by many metal reducing bacteria. Solid phase MnO_2 was chosen as the electron acceptor because it is representative of naturally occurring manganese oxides and can be easily synthesized in the lab. Growth and morphology of the biofilm was evaluated using confocal microscopy and/or a protein assay. The experiment was conducted at two flow rates. Initially, experiments were conducted at a flow rate that represented the average linear velocity of a fine to medium sand aquifer under natural gradient conditions. Four different experiments were conducted at this flow rate to determine variation within one experiment. A fifth experiment was conducted at a higher flow rate to imitate the average linear velocity of a coarse sand and gravel aquifer, and it was compared to the other four experiments. The redox equations for the chosen electron donors and acceptors are presented in Equations 1-3.

Oxidation of Acetate $$3H_2O + CH_3COO^- \rightarrow HCO_3^- + CO_{2_{(g)}} + 8H^+ + 8e^-$$ *Equation 1*

Reduction of Manganese $$16H^+ + 4MnO_{2_{(s)}} + 8e^- \rightarrow 4Mn^{2+} + 8H_2O$$ *Equation 2*

Overall Reaction $$CH_3COO^- + 8H^+ + 4MnO_{2_{(s)}} \rightarrow HCO_3^- + +CO_{2_{(g)}} + 4Mn^{2+} + 5H_2O$$ *Equation 3*

CHAPTER 2: METHODOLOGY

2.1 Materials

All materials were prepared under sterile conditions by first autoclaving and then handling in a Baker sterile hood. Manganese dioxide was used as the electron acceptor, and was prepared with $KMnO_4$, NaOH, and $MnCl_2 \bullet 4H_2O$, all from Sigma Aldrich with purities of ≥ 99%, ≥97%, and ≥ 99% respectively. Acetate was used as the electron donor, and was prepared with $NaCH_3COO$ from Sigma Aldrich with a purity of ≥99%. The sulfide for the media was prepared with Na_2S from Sigma Aldrich with a purity of ≥98% and the bicarbonate was added to the media as $NaHCO_3$ from Fisher Scientific with a purity of ≥99%. The argon used to maintain anaerobic conditions was Praxair with a purity of ≥99.995% and the nitrogen carbon dioxide mixture (80/20) used to constantly degas the media in the high flow experiment was distributed by Praxair with 80% nitrogen and 20% carbon dioxide.

2.1.1 Media preparation

The anaerobic media used in the experiments was buffered with bicarbonate and included sulfide, mineral solution, trace metals, vitamins, and selenium/tungsten at concentrations summarized in Table A.1 of Appendix A. This media contained 30 mM bicarbonate, and was degassed with a nitrogen/carbon dioxide mixture (80/20) to achieve a pH of 6.8. The media was autoclaved and then stored at 4°C, before being used at 25°C. Sulfide is a strong reductant, and was included primarily to act as an oxygen scavenger and reduce any oxygen that leaked into the system during reactor operation; it was added to the media immediately before introduction to the reactor to limit potential complexation with the trace metals that might happen during storage. A sulfide concentration of 50 µM was chosen in order to provide enough sulfide to act as an oxygen scavenger, but not enough to cause significant abiotic reduction of MnO_2. A control experiment confirmed that the sulfide did not contribute to manganese reduction over the experimental time scale.

Acetate was used as the electron donor at a concentration of 1 mM so that it would be in excess throughout the experiment and never limit the biological reactions (Calculation D.1, Appendix D). It was prepared using $NaCH_3COO$ and was added to the media with the other materials during the media degassing phase.

2.1.2 Manganese Dioxide Preparation

Manganese dioxide was synthesized according to procedures used by Villalobos et al. (2003) and Lovley & Phillips (1988). In this method, a 200 mM solution of $KMnO_4$ was slowly added with a syringe

over five minutes to a 486 mM solution of NaOH. A solution of 300mM $MnCl_2 \bullet 4H_2O$ was then added to that solution via syringe pump over 35 minutes. After 24 hours, the solution was concentrated and large cations were removed over five separate centrifuge and decanting cycles. The resulting manganese dioxide was colloidal δ - MnO_2 at a concentration of approximately 300 mM. The pH was not adjusted as outlined in the procedure by Villalobos et al. and was approximately 8.

The colloidal MnO_2 was used to coat Fisher Scientific fully frosted glass slides. The glass slides had dimensions of 2.54 cm x 7.62 cm x 1 mm and were frosted on one side, which aided with manganese attachment to the surface. The slides were massed initially, labeled in the top 0.5 cm, and the top 0.5 cm was then covered with labeling tape to ensure that there was some uncoated region of the slide that would be available for handling. Before coating the slides, the colloidal MnO_2 was stirred for 20 minutes on a stir plate to ensure that the colloidal particles were in suspension. Then the glass slides were coated by dispensing approximately 0.3 mL of colloidal MnO_2 onto the frosted surface using a plastic pipet. The MnO_2 was spread over the surface of the slide, and the excess MnO_2 was allowed to drip off the slide. After 24 hours of lying flat and air drying, the tape was removed from the slides and they were massed again to determine the actual mass of MnO_2 that had been retained.

Discrepancies with the mass balance for the initial experiments prompted measuring water content in the coated manganese. This involved massing coated slides and then leaving them in the oven at 105°C for 24 hours, and then remassing the slides. Changes in the mass indicated the water lost while in the oven.

2.1.3 Inoculum

Geobacter sulfurreducens strain PCA was used for reduction kinetics experiments. It was used because it is well-studied and has been shown to reduce manganese. *G. sulfurreducens* was cultured in the media described above with 1 mM acetate and 3 mM MnO_2 at a temperature of 25°C. In the cultures, MnO_2 was introduced as a colloidal form of manganese to help the bacteria adapt to MnO_2 as the electron acceptor. This culture was used for the inoculum at 2% of the volume of the influent media and acetate during a two-day inoculation phase. The cultures were maintained by adding more acetate and MnO_2, and were transferred to new media regularly to avoid a buildup of Mn^{2+} ions in the culture. All culture transfers and inoculum preparation work was conducted in a sterile hood to avoid contamination.

2.2 Flow-Through Reactor Setup and Operation

The experimental setup consisted of a vertical cylindrical flow vessel (Millipore stainless steel pressure filter holder, referred to as a reactor) inside a pseudo-airtight Plexiglas box that was constantly

purged with argon at a rate of 15 mL/min to maintain anaerobic conditions. Inside the reactor, the top 7.62 cm consisted of seven glass slides coated in MnO_2, which served as the electron acceptor, and the bottom 6.38 cm were filled with 5mm Pyrex solid glass beads to distribute flow (Figure 1).

The reactor, glass beads, metal reactor tubing, and slide holder were initially acid washed and rinsed with deionized water. The glass beads and slide holder were inserted into the reactor before autoclaving the reactor and reactor tubing with their open ends covered with aluminum foil. Any remaining plastic tubing was rinsed with HCl at a pH of 1, and then rinsed again with deionized water and dried with the ends covered. The reactor, tubing, and MnO_2-coated slides were then placed in the sterile hood and UV sterilized for 30 minutes. Inside the sterile hood, the MnO_2-coated slides were inserted into the reactor and the tubing was attached. The influent reactor tubing was attached to influent syringes, and effluent reactor tubing to a 500 mL collection bottle filled with 240 mL of 0.2 N HCl to quench further reaction (a 1 L collection bottle with 50 mL of 1.5 N HCl for the high flow experiment). All tubing connections were flame sterilized.

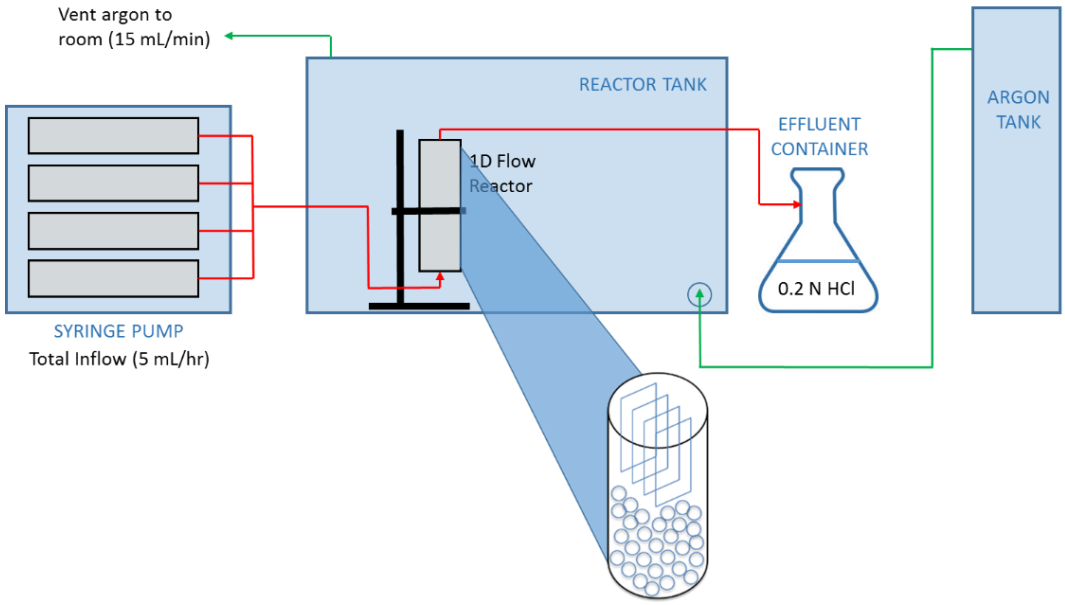

Figure 1. Experimental setup consisting of syringe pump, reactor tank, and effluent container. Glass beads and manganese dioxide coated slides are housed within the reactor.

A KD Scientific 230 syringe pump with four BD 60 mL luer lock syringes was used to deliver acetate amended media (with our without inoculum) through the reactor. All media was held in pressurized 120 mL bottles amended with sulfide to scavenge oxygen just before filling syringes in a sterile hood. The syringes were stored for several minutes with rubber stoppers on the ends of the needles to avoid contamination, and then connected to luer lock adapters on the reactor tubing and wrapped with Teflon

tape. The reactor was initially flushed with media containing 1 mM acetate for two days at a rate of 5 mL/hr. Next, the reactor was flushed with a 2% inoculum in media solution containing 1 mM acetate for two days at 5 mL/hr. The end of inoculation marked time zero for the experiment, and the reactor was then flushed with media containing 1 mM acetate for up to three weeks, or until the MnO_2 on the slides removed from the reactor was no longer visible. During this time, two different flow rates were evaluated in separate experiments: 5 mL/hr and 50 mL/hr. Because there are plans for future experiments at a lower flow rate, the 5 mL/hr and 50 mL/hr flow rates will be referred to as medium and high flow, respectively, for the remainder of this document. Four replicate experiments were run at medium flow, and only one at high flow. The medium flow rate (5 mL/hr) corresponds to a hydraulic retention time of 14.58 hours, and an average linear velocity across the slides of $1.5x10^{-6}$ m/s. Depleted 60 mL syringes were replaced with fresh ones approximately every two days in intermediate flow rate experiments, resulting in very brief (~10 min) flow interruption. In the high flow rate experiments, a Harvard Apparatus reciprocating syringe pump was used and the 60 mL syringes were refilled automatically from a large N_2-CO_2-sparged reservoir.

The first replicate experiment performed at 5 mL/min was used to determine when the glass slides should be removed from the reactor by evaluating changes in the effluent manganese concentration. For this reason, no slides were removed. In the remaining 5 mL/min experiments, the first slide was removed at least one week after inoculation. Depending on the color change of MnO_2 observed on the slide, the remaining slides were either removed at a rate of one per day or one every other day until all slides were removed from the reactor. Slides were removed from the reactor by pausing the syringe pump, clamping the influent tubing to prevent media flow, sterilizing tweezers with a Bunsen burner, removing the top of the reactor, and then extracting a slide with the tweezers. Slides were removed sequentially from the outside to the inside of the slide holder. After the final slide was removed, the media remaining in the reactor was drained and stored for analysis. All slides were stored in separate 100 mL media bottles filled with half media and half ethanol to fix the bacteria and prevent further growth.

2.3 Data Collection

The reduction kinetics were estimated using the manganese effluent concentrations. It was assumed that the manganese in the effluent was reduced in order to become mobile and leave the reactor and was therefore considered to be Mn(II) (Equations 1-3). Each effluent sample was tested for total manganese using ICP-MS. Samples were prepared with 2% nitric acid and evaluated in the linear region

of the standard curve. Raw ICP data is included in Appendix B. Manganese effluent for the fourth experiment was obtained with an ICP-MS, whereas the other experiments used an ICP-OES.

Each slide removed from the reactor was imaged on a Zeiss LSM 700 or 710 confocal microscope using a 63X oil objective. The slides were prepared by staining with SYTO 9 for 20 minutes in the dark and rinsing the slide with a 10X dilution of phosphate buffered saline (PBS). A small amount of PBS was then added to the slide surface with a plastic pipet and the slide was covered with a Ted Pella No. 1 large cover glass (1.96" x 2.95"). To prevent leakage of the PBS, clear nail polish was used to fix the slide to the cover slip on the edges. Images were collected with the confocal microscope at different depths within the biofilm sample, and then the two-dimensional images were stacked to create a three dimensional representation of the biofilm. SYTO 9 dye permeates into the cells and binds with nucleic acids in the cells, causing the dye to fluoresce when excited with lasers in the confocal microscope. The optimal thickness of the slices to obtain the best resolution was determined by the ZEN confocal software based on the thickness of the biofilm.

Confocal images were analyzed in two ways. First, ImageJ software was used to calculate the surface area covered by cells for the second and third experiments in each two dimensional image plane using threshold contrast (Rasband, 1997). Second, IMARIS visualization and analysis software was used to create a three dimensional surface around the fluorescent cells for the second, third, and fourth experiments, and the total volume of cells was estimated (Messerli, 1993). This total volume was divided by the volume of one *G. sulfurreducens* cell (approximately 0.39 μm^3 based on a cylinder of diameter 0.5 µm and length of 2 µm) and divided by the total glass slide area analyzed to estimate the total number of cells per glass slide.

In the second and third experiments, biomass on individual slides was also estimated using a colorimetric protein assay. For this, biomass was removed from each slide using a razor blade and by intermittently rinsing with sequential aliquots of media totaling 40 ml. A 10 mL subsample was taken from each 40 mL sample, and 3.33 mL of 1 M NaOH was added to the subsample to achieve a 0.25 N concentration of NaOH (Makkar et al., 1982). The samples were then heated in boiling water over a hot plate for ten minutes to extract proteins from the cells. Standards were treated similarly using an albumin protein standard. Samples and standards were prepared in 2 mL cuvettes by adding 50 µL of HCl to 1.975 mL of each sample or standard, to bring the pH into detectable spectrophotometer range. Exactly 10 minutes before measuring each sample and standard with a Shimadzu UV-2550 UV-VIS spectrophotometer at 595 nm, 1.975 mL of Coomassie (Bradford) reagent was added to each standard and sample. The samples were compared to the standard curve and their concentrations were estimated

using triplicate samples. The concentration of protein was then used to estimate the biomass on each slide.

2.4 Modeling Methods

The dual Monod kinetic model, shown in Equation 4, was initially considered to simulate changes in both electron donor and acceptor concentrations in the reactor. However, the effluent donor concentration was approximately equal to the influent donor concentration, and the equation reduced to the single Monod kinetic model shown in Equation 5. The Monod equation is appropriate for a completely mixed system. This condition was met because the characteristic time of the reaction was considerably longer than the characteristic time for advection and diffusion (Calculation D.2, Henze, 2008), resulting in little change in the acetate concentration (Calculation D.1, Appendix D). The rate of biomass growth is related to the rate of electron acceptor utilization as presented in Equation 6.

$$\frac{dEA}{dt} = -\mu_{max} * \frac{B}{Y} * \left(\frac{ED}{k_{ED}+ED}\right) * \left(\frac{EA}{k_{EA}+EA}\right) \quad \textit{[Concentration EA/time]} \quad \textit{Equation 4}$$

$$\frac{dEA}{dt} = -\mu_{max} * \frac{B}{Y} * \left(\frac{EA}{k_{EA}+EA}\right) \quad \textit{[Concentration EA/time]} \quad \textit{Equation 5}$$

$$\frac{dB}{dt} = \mu_{max} * B * \left(\frac{EA}{k_{EA}+EA}\right) - bB \quad \textit{[Concentration biomass/time]} \quad \textit{Equation 6}$$

Where,

$EA =$ concentration of electron acceptor in the system at time t (mass EA/volume)

$ED =$ concentration of electron donor in the system at time t (mass ED/volume)

$\mu_{max} =$ maximum specific growth rate (1/time)

$B =$ concentration of biomass (biomass/volume)

$Y =$ biomass yield ($biomass/mass\ of\ EA\ utilized$)

$k_{EA} =$ half velocity constant the electron acceptor (mass of EA/volume)

$k_{ED} =$ half velocity constant the electron donor (mass of ED/volume)

$b =$ decay constant (1/time)

In the single Monod equation, the rate of substrate utilization (Equation 5) and biofilm growth (Equation 6) are dependent on four main biological parameters (Rittmann & McCarty, 2001). These parameters are yield (Y), maximum specific growth rate (μ_{max}), the half saturation constant of the electron

acceptor (k_{EA}), and the decay constant (b). Yield is defined as the biomass produced per substrate utilized. The maximum specific growth rate is a ratio of the most rapid rate of growth to the biomass in the system at that rate of growth. And the half saturation constant is the amount of substrate that has been converted when the specific growth rate is at half the maximum. Because the biomass data for these experiments did not indicate significant decay, it was assumed to be zero in the model.

Equations 5 and 6 were modified for the experimental system to be in units of cells of *G. sulfurreducens* and mmoles of MnO_2. This resulted in Equations 7 and 8, respectively. This was done to allow for the use of mass units instead of concentration units because mass units are needed when evaluating biofilm growth on a solid surface. The biomass and yield values were converted to cells of *G. sulfurreducens* and cells of *G. sulfurreducens* per mmol MnO_2, respectively, using the assumption that each cell was 0.2 picograms.

Change in manganese over time:

$$\frac{dMnO_2}{dt} = -\mu_{max} * \frac{B}{Y} * \left(\frac{MnO_2}{k_{MN}+MnO_2}\right) \qquad \textit{Equation 7}$$

Change in biomass over time:

$$\frac{dB}{dt} = \mu_{max} * B * \left(\frac{MnO_2}{k_{MN}+MnO_2}\right) \qquad \textit{Equation 8}$$

Where,

$MnO_2 = \text{mass of } MnO_2 \text{ remaining in the reactor at time t (mmol } MnO_2)$

$\mu_{max} = \text{maximum specific growth rate } (1/\text{hr})$

$B = \text{mass of biomass (cells)}$

$Y = \text{biomass yield (cells/mmol } MnO_2 \text{ reduced)}$

$k_{MN} = \text{half velocity constant of } MnO_2 \text{ (mmol } MnO_2)$

Equations 7 and 8 were solved numerically in MATLAB with a first order solution that is explicit in time and with a small time step (Δt) of one hour. A small time step was used so that the results were not sensitive to this increment. New biomass was first calculated at each time step using Equation 9, and then the amount of manganese reduced was calculated with Equation 10.

Biomass at time t:

$$B_t = B_{t-1} + \frac{dB}{dt} * \Delta t \qquad \textit{Equation 9}$$

MnO_2 at time t:

$$MnO_{2_t} = MnO_{2_{t-1}} + \frac{dMnO_2}{dt} * \Delta t \qquad \textit{Equation 10}$$

The numerical solution to Equation 7 was validated by comparing to the analytical solution in Equation 11, which assumes a large and constant biomass. Equation 11 was determined according to Calculation D.4 in Appendix D. When the biomass is constant, μ_{max}*(B/Y) becomes a single constant (hereafter referred to as A), and the Monod equation only depends on the two constants A and k_{MN}.

$$A * t = k_{MN} * log\left(\frac{Mn_0}{Mn}\right) - Mn + Mn_0 \qquad \text{Equation 11}$$

Where,

$t =$ time since begining of manganese degradation (hr)

$Mn_0 =$ the inital MnO_2 mass (mmol MnO_2)

$Mn =$ the MnO_2 mass remaining at time t (mmol MnO_2)

CHAPTER 3: RESULTS

3.1 MnO_2 Reduction Kinetics

The manganese effluent concentration and flow rate were used to calculate the mass of manganese leaving the reactor over time, normalized for one representative slide. This mass presents $1/7^{th}$ of the initial mass actually in the reactor because the mass balance analysis was completed for only the last slide removed from the reactor, assuming the rate of MnO_2 removal from all slides was the same. The results are plotted in Figure 2, and raw data for manganese concentrations and effluent volumes are included in Table B.1 in Appendix B for all four medium flow (MF) experiments and the one high flow (HF) experiment.

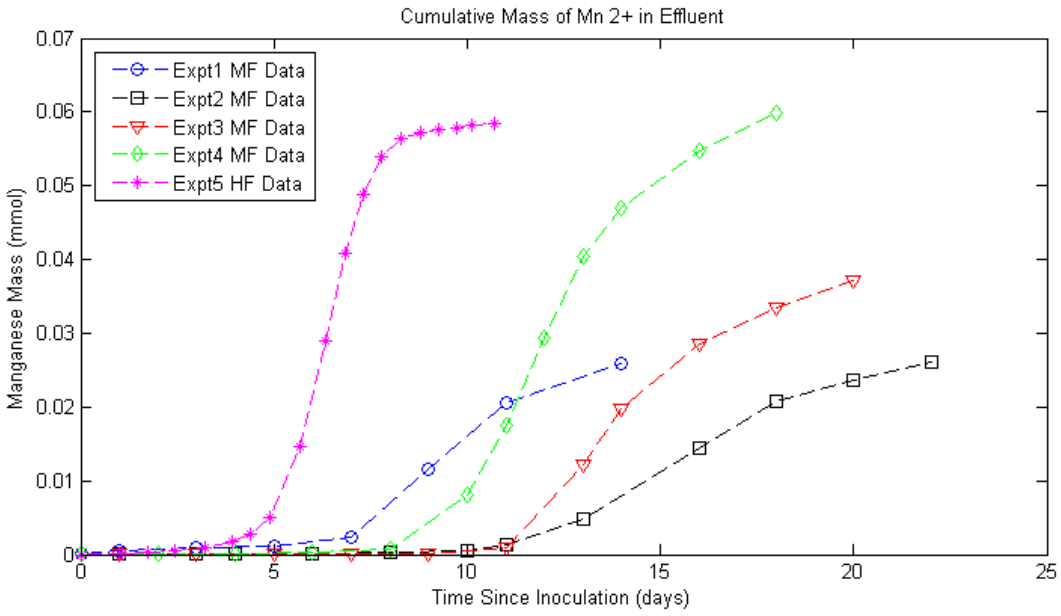

Figure 2. Manganese effluent data. MF denotes medium flow, 5 mL/hr and HF denotes high flow, 50 mL/hr.

The rate of manganese mass leaving the reactor did not increase until after a lag phase that lasted 7 to 11 days for the MF experiments and 4 days for the HF experiment. After this initial lag phase, the rate of manganese release increased and then decreased (Figure 2). The four MF experiments show variable curves; their lag time, curve steepness, and cumulative manganese mass are different. Based on the one completed HF experiment, it appears as though higher flow rates contribute to faster reduction because the curve is steeper, but more experiments would be needed to support this.

Table 1 presents the maximum slope of each experiment which was determined by taking the two data points on the steepest portion of the curve and determining the ratio of the change in manganese to the change in time. The fifth experiment with high flow had the steepest slope of 2.28×10^{-2} mmol

MnO_2/day, which was more than twice as steep as the steepest slope of $9.94x10^{-3}$ mmol MnO_2/day in the medium flow experiments. All four MF curves fall within the same order of magnitude with an average slope of $6.03x10^{-3}$ mmol MnO_2/day and a standard deviation of $3.38x10^{-3}$. The high flow experiment slope is more than three standard deviations greater than the average of the slopes from the MF experiments. Because the fifth experiment was sampled every twelve hours and the other four experiments were sampled every 1-2 days, it is possible that the maximum slope was not captured in the first four experiments. But despite the difference in sampling, the slopes of the MF experiments are unlikely to increase by multiple standard deviations and will still be significantly less steep than the high flow experiment.

3.2 MnO_2 Reduction Mass Balance

The initial mass of manganese coated on one representative slide in each reactor experiment is presented in Table 1 (Calculation D.3, Appendix D). Eight control slides were coated and placed in the oven to estimate the water trapped in the colloidal manganese. The average water content in these slides was 8.82% (Table B.2 and Figure B.1, Appendix B). The initial Mn increased with experiment number; this was not intended and may be due to better MnO_2 coating procedures developed over time.

Table 1. Experimental data for mass balance and maximum slope of reduction. Due to the mass balance exceeding 100% for Experiment 4 when the water content was included, modeling efforts used the initial mass on the slides without water content included.

Experiment	**Initial Mass on Slides – Water Content Ignored (mmol)**	Initial Mass on Slides - Water Content Accounted For (mmol)	Mass of Manganese in Effluent (mmol)	Maximum Slope (mmol MnO_2/day)	**Mass Recovered - Water Content Ignored (% of initial mass)**	Mass Recovered - Water Content Accounted For (% of initial mass)
1	**0.0363**	0.0331	0.0259	$4.54x10^{-3}$	**72%**	78%
2	**0.0419**	0.0382	0.0285	$2.18x10^{-3}$	**68%**	75%
3	**0.0514**	0.0469	0.0363	$7.45x10^{-3}$	**71%**	77%
4	**0.0592**	0.0540	0.0556	$9.94x10^{-3}$	**94%**	103%
5	**0.0744**	0.0678	0.0599	$2.28x10^{-2}$	**78%**	88%

The manganese effluent concentration and flow rate were used to calculate the mass of manganese leaving the reactor over time, again normalized for one representative slide. This is plotted in Figure 2, and the total manganese mass in the effluent is presented in Table 1.

Based on the manganese mass in the effluent, the mass balance for the five experiments ranged from 68%-94% (Table 1). When no slides were removed from the reactor in the first experiment, the mass

balance was 72%; this means that the disruption from opening the reactor and removing the slides was not the sole contributor to discrepancies in the mass balance. A summary of when slides were removed from the experiments is given in Table 2. The significantly higher mass balance observed with the fourth experiment was the result of experimental variation, not analytical methods.

Mass balance errors could be due to error in estimating the cumulative mass in the effluent, neglecting to account for trapped water in the manganese initially, issues with the scale when estimating initial mass, or impurities in the colloidal manganese from synthesis. The mass in the effluent was estimated from the initial ICP data (Table B.1, Appendix B) to account for the mass removed from the system when slides were removed. This was done by adding a fraction of the mass that would have been reduced if all seven slides were present in the reactor back into the effluent mass. For example, if one slide had been removed from the reactor, the effluent mass would be multiplied by (1+1/6), meaning that an extra 1/6th of the mass in the effluent would have existed if all seven slides had been present in the reactor. This approach assumes that the mass on the slides is the same and that all seven slides are reducing at the same rate, which is an overarching assumption for the whole experimental method.

Table 2. Summary of slide removal for each experiment.

		Experiment 1	Experiment 2	Experiment 3	Experiment 4	Experiment 5
		5 mL/hr (medium)	5 mL/hr (medium)	5 mL/hr (medium)	5 mL/hr (medium)	50 mL/hr (high)
Days Since Inoculation (Slides Noted on Day Removed)	6	No Slides Removed in this Experiment	Slide 10			
	7					Slide 3
	8		Slide 3			Slide 6
	9			Slide 10	Slide3	Slide 12
	10		Slide 9			Slide 11
	11				Slide 10	Slides 9, 8, and 7
	12				Slide 9	
	13			Slide 2	Slide 4	
	14		Slide 8	Slide 9		
	15				Slide 5	
	16		Slide 5	Slide 4		
	17				Slide 8	
	18			Slide 5		
	19				Slide 7	
	20		Slide 7	Slides 8 and 6		
	21					
	22		Slide 6			

Another potential source of error was the water content in the manganese. Although this was not accounted for when estimating the initial mass, the percent of water is highly variable from slide to slide (Table B.2, Appendix B), which makes it difficult to assume that every slide had 8.82% of water making up

its total mass. Also the mass balance differs by significantly more than 8.82% for some experiments, so this would not completely account for the discrepancies. Figure 3 represents the possible range of initial manganese masses when up to 8.82% of the mass measured on the scale is water.

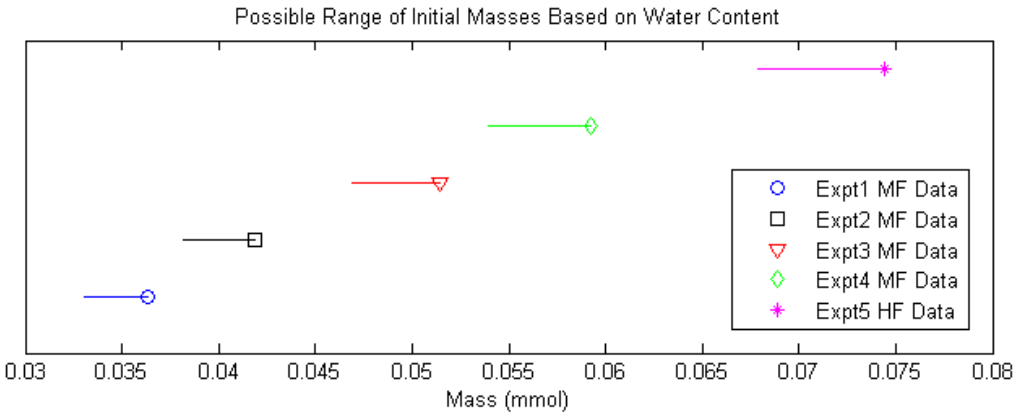

Figure 3. Range of possible manganese initial masses. Data points indicate the measured amount of initial manganese and the lines represent lower values of manganese that could have possibly been introduced based on an 8.82% water content.

The scale used to determine the initial mass of manganese may have also contributed to the error in the mass balance. Assuming the scale was accurate to ±0.1 mg, each slide could have had a percent error in the mass estimate between 1-3%, depending on the magnitude of the mass on the slide. A microscale would have been useful to ensure accuracy in these measurements.

Finally, the poor mass balances could be due to impurities in the manganese dioxide. For example, if manganese mineral phases other than MnO_2 existed in the colloidal manganese that had a higher molecular weight than MnO_2, the amount of manganese in the system would be overestimated. To check this potential source of error, Raman spectroscopy was used to determine which mineral phase(s) were present on a MnO_2-coated slide, and results are presented in Figure 4. Only MnO2 is present, suggesting this is not the source of error.

Despite the issues with the mass balance, the maximum specific growth rate and the yield can still be estimated from this data set and can be used in models to determine the half saturation constant.

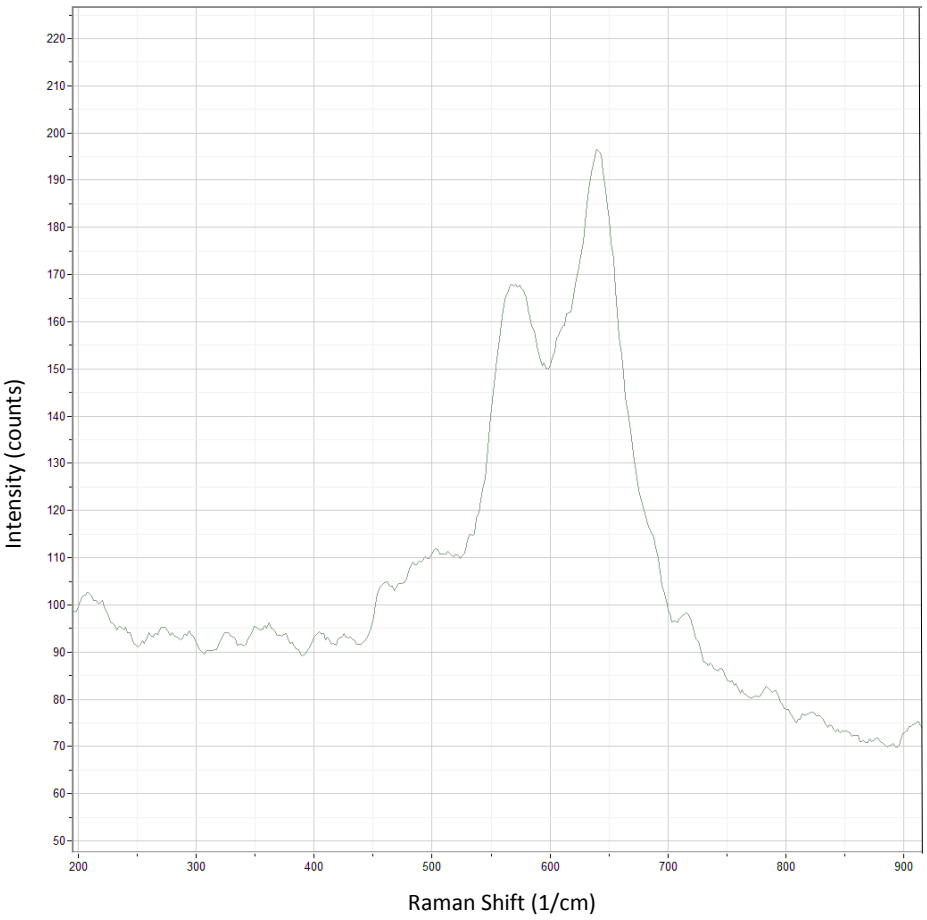

Figure 4. Raman spectra of manganese dioxide taken from a coated slide.

3.3 Laser Confocal Imaging Results

Confocal images of microorganisms in biofilms are shown in Figure 5, and are indicated by fluorescent regions. The images are two dimensional projections of three dimensional cell distributions. An increase in area showing fluorescence over time indicates biofilm growth. At early times, the biofilm showed sparse coverage before reaching the exponential growth phase (Figure 5.A). During periods of increased biofilm growth, colonies were seen in the second and fourth experiments (Figure 5.B), and mushroom structures were captured in the third experiment (Figure 5.C). Later time morphologies for all experiments were characterized by increased density of the biofilm (Figure 5.D). All of the images for the different experiments can be found in Appendix C. Limited data was compiled for the second and third experiment; only two images were taken for each slide at only three time points. For the fourth experiment, six images were taken of the slide at six different points depicted in Figure 6. A data set of images similar to the fourth experiment has yet to be compiled for the fifth experiment.

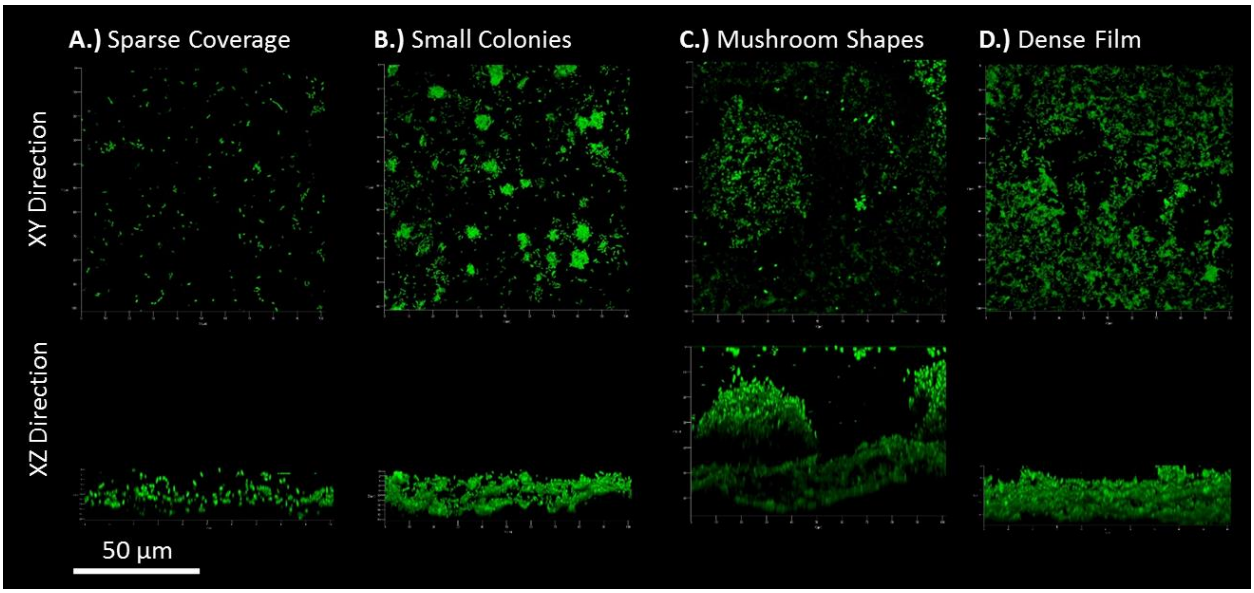

Figure 5. Different types of morphologies imaged with the confocal microscope across the different experiments.

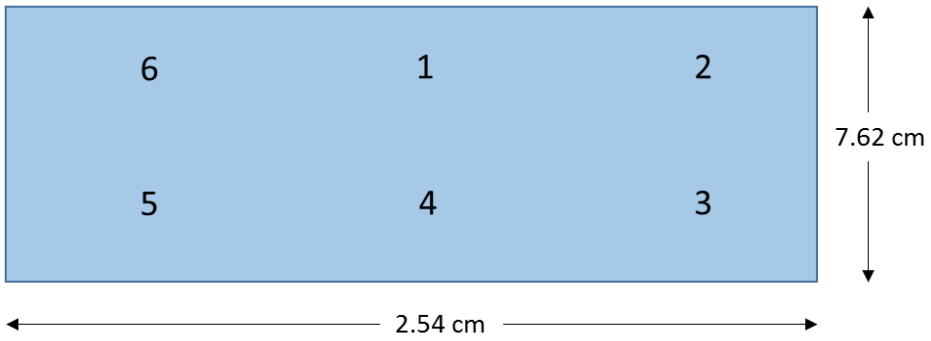

Figure 6. Locations where images were taken on each slide in the fourth experiment.

Fluorescent biomass in confocal images was initially quantified using ImageJ (Rasband, 1997) to determine the area of the images covered with cells (Figures C.3 and C.4, Appendix C). Based on the area covered by *G. sulfurreducens* cells at early times, a cell count was estimated for denser biofilm images. Table 3 presents the cell count estimates. There was concern that ImageJ was not accurately depicting the amount of biomass because two-dimensional images may not capture out of plane microorganisms. Therefore, IMARIS (Messerli, 1993) imaging software was used to evaluate the confocal data sets in three dimensions. The volumes estimated from IMARIS for each slide were used to estimate cell counts. Table C.1 in Appendix C summarizes the volumes and associated cell counts for each confocal Zstack image in the fourth experiment and Table 3 compares IMARIS data to ImageJ data. With IMARIS, six images for each slide were averaged to estimate the cell count and the trend in cell growth was fit with a polynomial (Figure 7). This data was used to determine trends in yield and maximum specific growth rate over the

course of the fourth experiment. This same analysis was not possible for the second and third experiments because limited image data was collected. However, the few images available were evaluated for cell count and compared to the protein assay to support use of images for cell count estimates (Table B.1, Appendix B).

Table 3. Methods to estimate biomass. ImageJ uses 2D images, IMARIS uses 3D images, and the protein assay is determined with absorbance. Gray cells show a comparison of IMARIS to the protein assay.

Experiment 2

		Cell Count		
Number	Days Since Inoculation	ImageJ	IMARIS	Protein Assay
Slide 10	6			
Slide 3	8	9.45E+07	2.65E+08	
Slide 9	10			
Slide 8	14	1.49E+08	2.34E+08	**3.90E+08**
Slide 5	16			**1.08E+09**
Slide 7	20			**1.21E+09**
Slide 6	22	3.62E+08	4.03E+08	**1.28E+09**

Experiment 3

		Cell Count		
Number	Days Since Inoculation	ImageJ	IMARIS	Protein Assay
Slide 10	9	6.99E+07	1.47E+08	
Slide 2	13	7.86E+08		**9.87E+08**
Slide 9	14		4.04E+08	**8.72E+08**
Slide 4	16	2.90E+08		**7.64E+08**
Slide 5	18			**1.16E+09**
Slide 8	20	8.53E+08	1.50E+09	**1.26E+09**
Slide 6	20			**1.19E+09**

Experiment 4

		Cell Count - IMARIS		
Number	Days Since Inoculation	Images	Std Dev.	From Trendline
Slide 3	9	7.73E+07	2.09E+07	2.72E+08
Slide 10	11	1.07E+09	3.76E+08	6.35E+08
Slide 9	12	5.64E+08	2.49E+08	7.88E+08
Slide 4	13	1.02E+09	2.21E+08	9.22E+08
Slide 5	15	1.18E+09	1.29E+08	1.13E+09
Slide 8	17	9.09E+08	2.66E+08	1.27E+09
Slide 7	19	1.52E+09	1.38E+08	1.32E+09

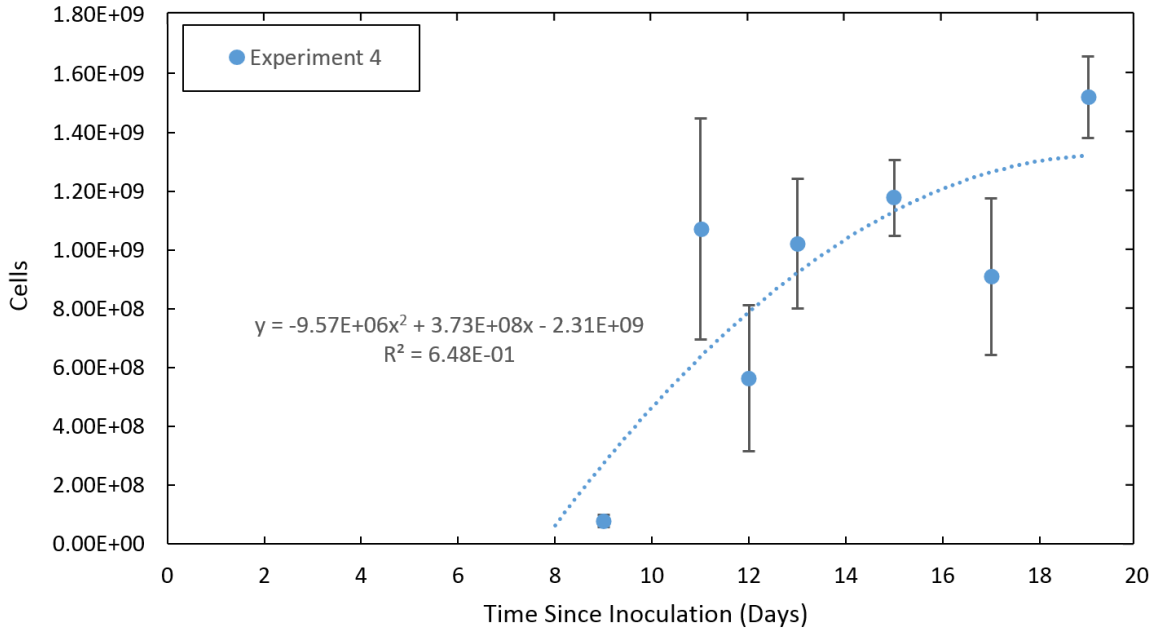

Figure 7. Biomass data quantified using surfaces and volumes in IMARIS for the fourth experiment.

The cell counts estimated with IMARIS are always larger than with ImageJ. The ImageJ cell counts vary from 10-65% less than the IMARIS cell counts. Because of this, it is assumed that the IMARIS data is more accurate than the ImageJ data. There are only three or four data points for ImageJ and IMARIS for both the second and third experiments because limited confocal images were compiled for these two experiments. More data was collected for the fourth experiment, which allowed the inclusion of error bars and a simple polynomial fit to the biomass growth data (Figure 7). It is difficult to describe trends in the biomass data with the limited data points in the second and third experiments, which is why future experiments will focus on collecting more confocal data like the fourth experiment.

3.4 Protein Assay results

The accuracy of the cell estimates with the images was determined by comparing them to the protein assay. The concentration of protein for each slide removed from the reactor was determined, and a cell count was estimated using the assumptions that each *G. sulfurreducens* cell has a weight of 0.2 picograms and that protein accounts for 50% of the mass of each cell (Figure 8). Three samples from the same 10 mL subsample were evaluated on the spectrophotometer, which make up the error bars in Figure 7. The protein assay data for the second experiment shows an increase in cells over time throughout the experiment, but the data for third experiment shows a decrease in cells from days 13 to 16 and then an increase from days 16 to 20. The error bars represent data precision since they represent the standard deviation of multiple measurements from the same sample. Measures of protein for different protein

extracts were not performed. The method detection limit is approximately 1 µg/mL. The measured data points are close to the detection limit as shown in Figure 9. Raw data for the protein assay is included in Table B.1 in Appendix B.

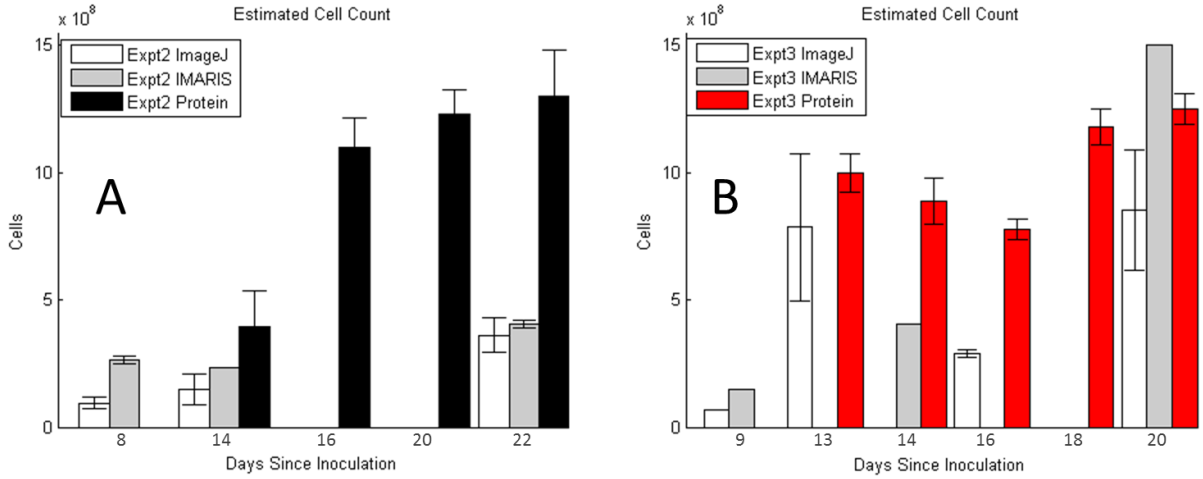

Figure 8. Comparison of protein assay to ImageJ and IMARIS analysis. A is data from the second experiment, and B is data from the third experiment. Error bars only included when more than one data point was available to calculate the standard deviation.

The protein assay showed higher cell counts than the image analysis for all data points except day 20 in the third experiment, where IMARIS data showed a higher cell count (Table 3, Figure 8). It is difficult to discuss the trends in data sets relative to each other because of the large or nonexistent error bars. The image estimates, both with ImageJ and IMARIS were on the same order of magnitude as the protein assay data, and showed similar trends for the most part.

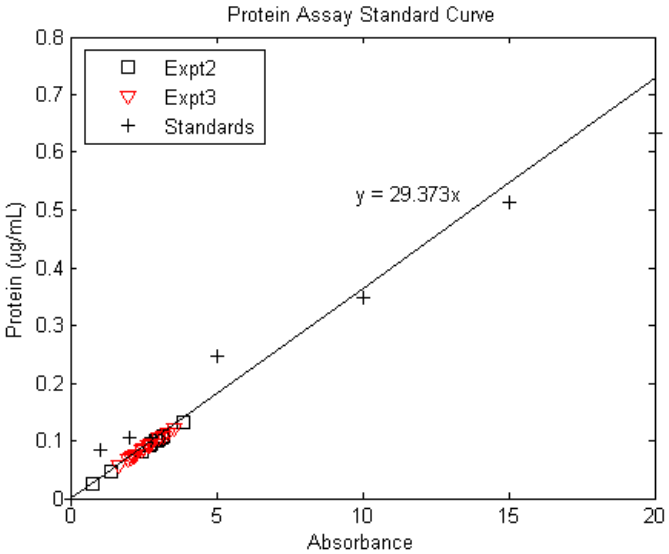

Figure 9. Protein assay standard curve. Note the proximity of the data points to zero absorbance.

3.5 Modeling Results

3.5.1 Model validation

The analytical solution is compared to the numerical solution using a large constant biomass of $1x10^9$ cells in Figure 10. The two profiles lie on top of each other, validating the numerical model solution. The analytical solution is compared to the numerical model in Figure 11, when the latter has increasing biomass growth over time. Faster growth is observed with the numerical model because there are more cells in the system, which allow for a faster rate of reduction.

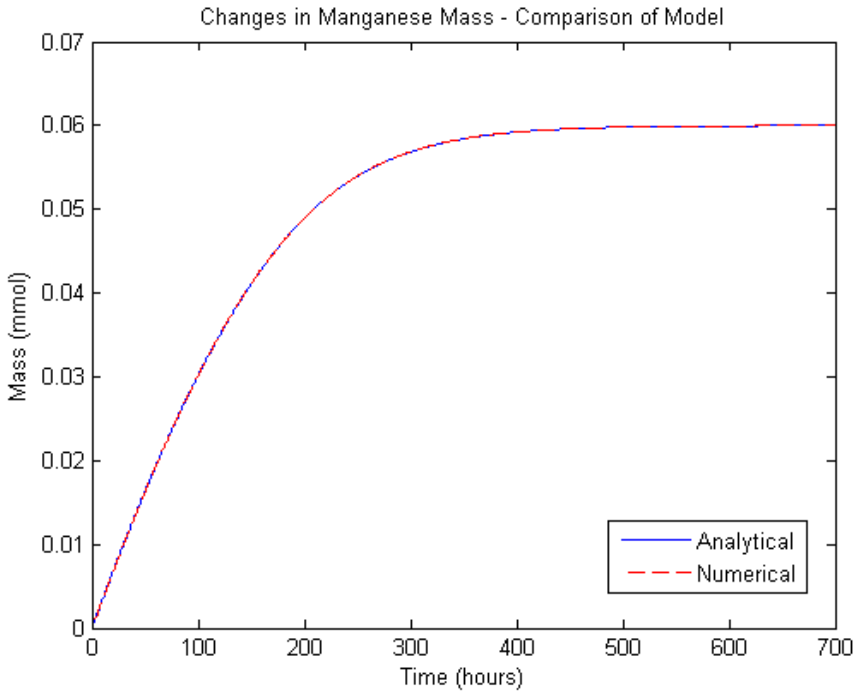

Figure 10. Numerical model validation ignoring biomass growth and comparison to analytical solution. The curves are the same when biomass is assumed constant for both solutions.

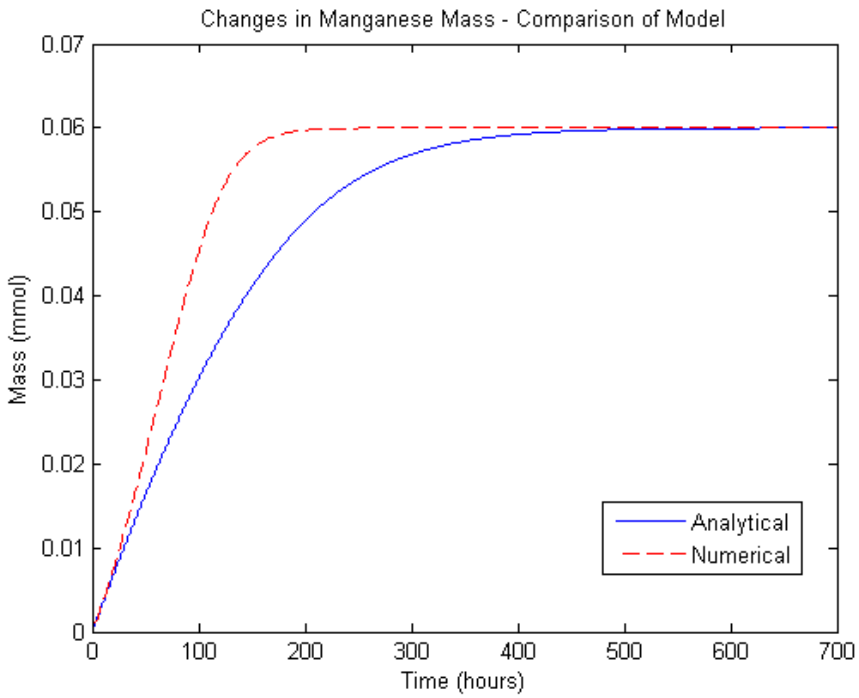

Figure 11. Numerical model validation using analytical solution. This figure represents the difference of the numerical solution that includes biomass growth and the analytical solution that assumes constant biomass.

3.5.2 Parameter estimation

Yield (Y) and maximum specific growth rate (μ_{max}) were estimated from the manganese effluent and protein assay data from the second and third experiments and with the IMARIS data from the fourth experiment. Yield is the ratio of the change in biomass to the change in substrate utilized; μ_{max} is the ratio of the maximum slope in the biomass growth curve to the amount of biomass at the tangent to that curve (Figure 12, Equations 12 and 13).

$$Y = \frac{m_2 - m_1}{Mn_2 - Mn_1} \qquad \textit{Equation 12}$$

$$\mu_{max} = \frac{\frac{m_2 - m_1}{t_2 - t_1}}{m_{@max}} \qquad \textit{Equation 13}$$

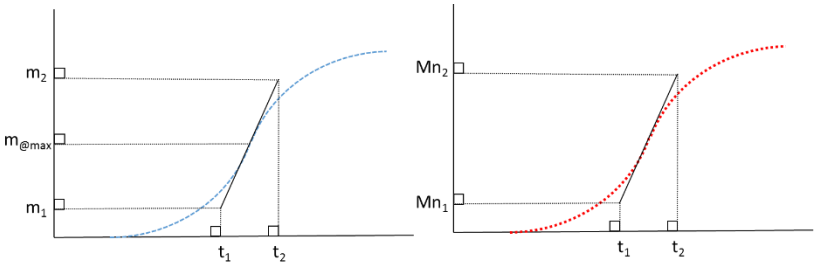

Figure 12. Definition of maximum specific growth rate and yield. m is the biomass and Mn is the mass of manganese in the effluent. t is the time since inoculation.

The yield and maximum specific growth rate were estimated from experimental data and used in the model. The data for biomass and manganese effluent are summarized in Table B.1, Appendix B, and

were used to determine the biomass yield and μ_{max} for all four experiments. IMARIS data was used for cell counts at early time where protein assay data was below the detection limit in the second and third experiments. Because of limited and error-prone biomass data, the calculated yield and μ_{max} are only estimates. These calculations resulted in a range of yield values, with an average of 3.44×10^{10} cells/mmol for the MF experiments. The specific growth rates were calculated for the second and third experiments using the protein assay data, and μ_{max} was determined to be 0.0196 1/hr and 0.0155 1/hr respectively. The μ_{max} estimated from the trendline related to the IMARIS data for the third experiment was 0.0167 1/hr. Because the largest value of the maximum specific growth rate determined from any of the three experiments with biomass data was 0.0196 1/hr, this value was chosen to guide the choice of μ_{max} for the model. This was rounded up to 0.02 1/hr for the model calculations.

3.5.3 Comparison of Model to Experimental Data

The numerical model was used to fit the experimental data using a yield of 3.44×10^{10} cells/mmol MnO_2 and a maximum specific growth rate of 0.02 1/hr estimated from the experiments. The initial biomass and k_{MN} were used as fitting parameters. Figures 13.A and 13.B present a comparison of the experimental data and the numerical model. There is a poor fit of manganese effluent at late time for the first, second, and third experiments, which may be due to the incomplete mass balance for these experiments. Errors between the model and the data are presented in Figure 13.C for manganese, and Figure 13.D for cell count. Errors are defined as the absolute value of the difference between the experimental data points and the model data points at the same time. The error in cell count by the model is likely due to natural variability in biofilm growth and imprecise measurements of biomass with the protein assay. The model may more accurately reflect the amount of biomass in the system because biomass was likely lost during confocal slide preparation and removal of biomass from the slide, resulting in an underestimation of the actual biomass present.

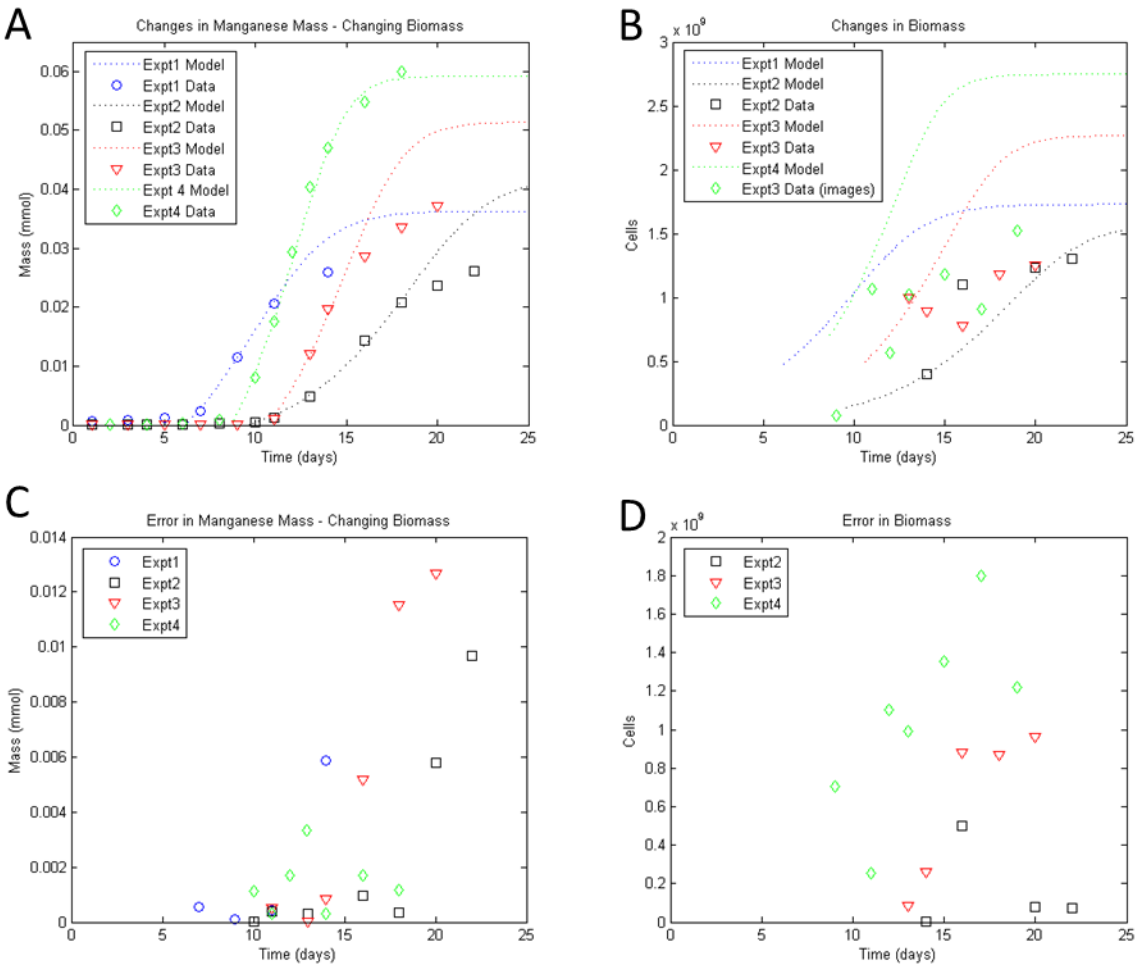

Figure 13. Curve fitting for medium flow experiments using numerical model with experimentally determined yield and maximum specific growth rate. A is the manganese curve fitting, and B is the biomass curve fitting. C and D are the error for the manganese and biomass curve fitting, respectively.

Best fit model parameters are in Table 4. The initial biomass, which impacts the steepness of the model slope (especially at early times), is greatest for the fourth experiment, which has the greatest initial mass of manganese. The first and second experiments do not show an increasing slope with increasing initial manganese, which may only be more apparent at larger total initial masses. The half saturation constant estimated from the model fitting is 0.04 mmol, which means that as the electron acceptor is exhausted, the kinetics transition from zero-order to first order (Equations 7-10). This makes sense because k_{MN} has a greater impact on the steepness of the late time slope. A summary of the model at different values of the important parameters is included in Figure E.1 in Appendix E.

Table 4. Parameters used to fit medium flow experimental data.

Parameter	Symbol	Source	Value
Yield	Y	Experiments 2, 3, & 4	3.44×10^{10} cells/mmol
Maximum Specific Growth Rate	μ_{max}	Experiments 2, 3, & 4	0.02 1/hr
Initial Biomass	B_0	Fitting Parameter	Expt1: 4.8×10^8 cells
			Expt2: 1.4×10^8 cells
			Expt3: 5.0×10^8 cells
			Expt4: 7.1×10^8 cells
Half Maximum Velocity Constant for Manganese	k_{MN}	Fitting Parameter	0.04 mmol

This same curve fitting exercise was done for the high flow experiment using the experimentally determined yield and μ_{max}. Because there is only one experiment, the curve fitting is not constrained as well as for the medium flow experiments. Assuming an initial biomass of 9×10^8 cells, the k_{MN} was estimated to be 0.01 mmol (Figure 14). This value is significantly smaller than the k_{MN} estimated for the medium flow experiments, which means that the reaction rate will more closely follow zero order (Equations 7-10).

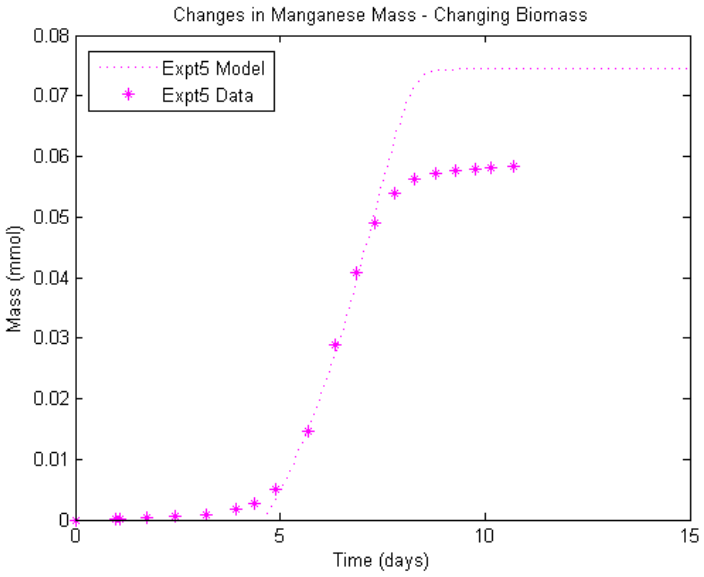

Figure 14. Curve fitting for high flow experiments using the numerical model. Deviation of the model from the experimental data points is due to only achieving a 78% mass balance for the fifth experiment.

CHAPTER 4: DISCUSSION

The methods described to evaluate the kinetics of reduction of MnO_2 by *Geobacter sulfurreducens* in a flow through system involved collecting manganese effluent data and biomass data over a two to three week experimental period, estimating Y and μ_{max} from this data, and then fitting the experimental data with a Monod-based model to estimate initial biomass and k_{MN}.

A yield of 3.44 cells/mmol MnO_2 was calculated, and it is approximately twice as large as the value of 1.75 cells/mmol MnO_2 estimated by Roden and Jin from an energetics-based approach that correlated Gibbs free energy to yield (2011) (Calculation D.5 in Appendix D). The standard deviation in the value of yield calculated for the first four experiments showed that the actual yield could be $3.44x10^{10} \pm 2.54x10^{10}$ cells/mmol MnO_2, a range which includes the yield presented by Roden and Jin. Because there was considerable error with the biomass estimate from the model in Figure 13.D, the value of yield determined by Roden and Jin was also tested in the model. There was significantly less error in the biomass when the smaller value of yield is used (Figure 15). It is possible that there is a better way to estimate yield than taking the average of all the different yield values calculated between each data point (Table A.2, Appendix A).

A μ_{max} of 0.02 1/hr was determined from the experiments, which is half of the μ_{max} of 0.04 1/hr presented in the literature by Holmes et al. for reduction of MnO_2 by *G. Sulfurreduccens* with acetate as the electron donor (2013). Because μ_{max} is the ratio of the maximum slope of the biomass vs. time curve to the biomass at that maximum slope, it is possible that the experiments underestimated the maximum slope due to inadequate biomass sampling. One could also explain the lower μ_{max} by assuming that the protein assay overestimated the biomass on the slides. This is less likely than missing the maximum slope in sampling because an underestimation of biomass is more probable after the extraction of the slides and the handling involved with confocal image preparation and removal of biomass for the protein assay. Although it is possible that the value of 0.2 picograms per geobacter cell is an underestimate of the cell mass initially, which could overestimate total biomass.

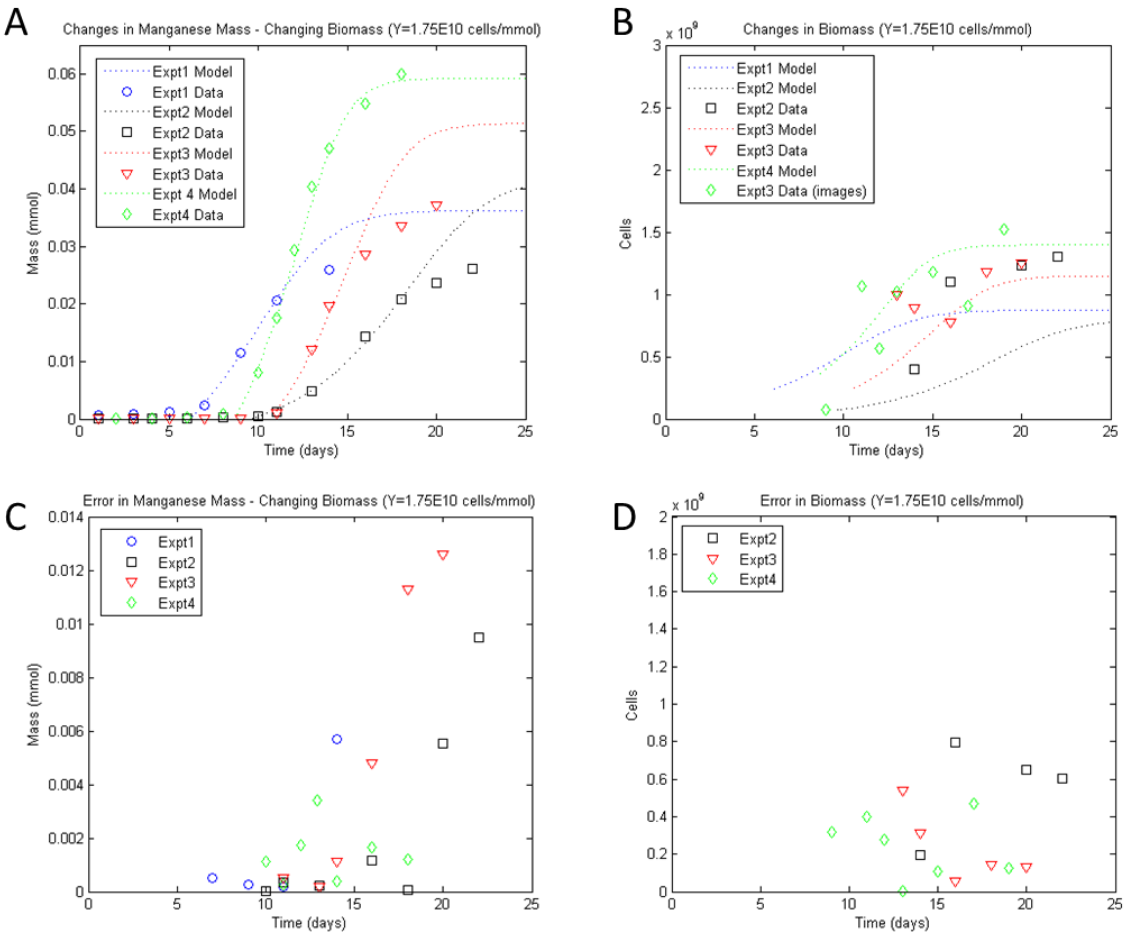

Figure 15. Curve fitting for medium flow experiments using numerical model with experimentally determined maximum specific growth rate and the yield from Roden and Jin (2011). A is the manganese curve fitting, and B is the biomass curve fitting. C and D are the error for the manganese and biomass curve fitting, respectively.

Literature values of k_{MN} for reduction of solid phase manganese were not found. Most available data for half saturation constants exists for solution phase electron acceptors, not solid phase such as MnO_2. Although literature data for the half saturation constant of MnO_2 could not be found, the modeling results were compared to the half saturation constant of ferric citrate because iron and manganese often behave similarly in a natural environment. The estimation of 0.04 mmol for k_{MN} at the medium flow rate determined from fitting the model to the experimental data is slightly larger than the k_{Fe} of 0.033 mmol calculated from Liu et al. (2002) for geobacter and acetate assuming a reactor volume of 73 mL (which was the void space calculated for the flow-through reactor). This value of k_{MN} could be useful for other studies as an estimate of the half saturation constant when solid phase MnO_2 is the electron acceptor.

The k_{MN} at the low flow rate was 0.04 mmol and at the high flow rate, for the one completed experiment, it was estimated to be 0.01 mmol. According to Mulder & Hendriks (2014) the half saturation

constant can be impacted by environmental conditions and relates to the efficiency of the organisms and how well-adapted they are to their environment. Low half saturation constants often apply to organisms that can be efficient with resources at low concentrations and densities, whereas larger half saturation constants are indicative of less efficient organisms. According to the parameters estimated from the experiments, k_{MN} is larger for the slow flow rate, which would indicate that at slower flow rates the *G. sulfurreducens* are less efficient.

It is possible that the higher flow rates result in faster mass transfer because the boundary layer is smaller, which would explain the difference in k_{MN} values between the high and medium flow experiments. It is also possible that the effective yield in the fifth high flow experiment may be less than what was estimated for the medium flow experiment due to shear removal of biomass in the higher flow system. If the effective yield is less in the high flow experiments, a higher k_{MN} would have been necessary to fit the data, resulting in no difference in k_{MN} between the experiments and instead a difference in yield. A biomass estimate needs to be obtained for the fifth experiment to determine if the yield is significantly different than the medium flow experiments. A similar check should be conducted for the maximum specific growth rate.

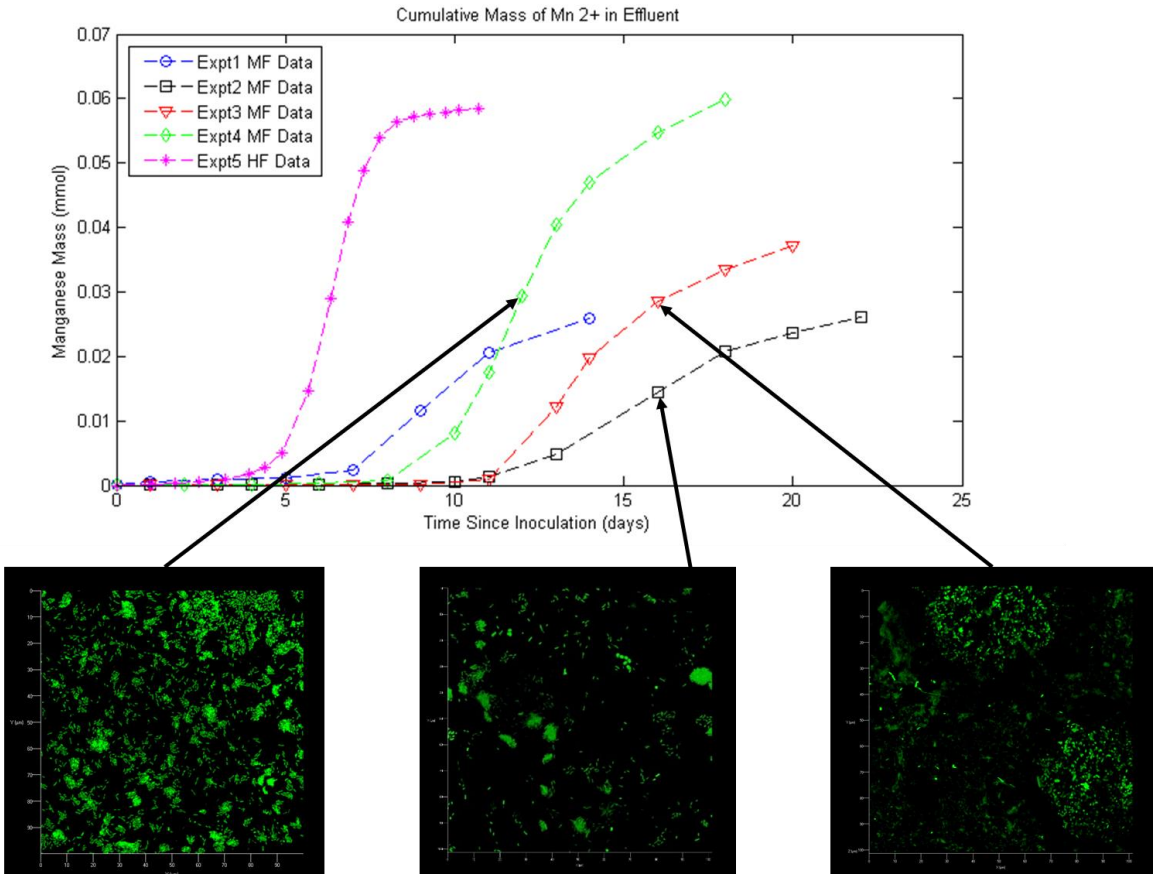

Figure 16. Morphology at maximum reduction rate for experiments 2-4.

More data is necessary to reach this work's main goal of evaluating the interaction of flow rate, morphology, and reduction kinetics. There was a loose relationship to biofilm morphology and reduction kinetics seen within a single experiment. Colonies tended to form near points in time that correlated with the maximum rate of reduction (Figure 16). Although the types of colonies vary from sparse colonies in the second experiment, to denser colony formation in the fourth experiment, to mushroom-shaped colonies in the third experiment, the grouping of cells may be important. It is possible that colony formation is correlated to faster rates of reduction, or that colonies begin to form when the substrate becomes limited. With more images from future experiments, it may be possible to make stronger correlations between flow rate, morphology, and reduction kinetics.

Based on the results, there are advantages and disadvantages to this experimental approach. First of all, this approach makes it possible to estimate a half saturation constant for a solid phase electron acceptor, which is limited in the literature. Second, the experimental set up allows qualitative data related to the biofilm structure to be determined using a confocal microscope, and allows for the estimation of biomass using either a protein assay or an image analysis. The disadvantages of this approach are the

underlying assumption that every slide in the reactor is uniform and reducing at similar rates, and the limited biomass data that is available. In a batch system with soluble electron acceptors, the biomass can be estimated using optical density, which allows for the possibility of more data points than the reactor in this study that only has seven slides, and by default only seven biomass data points. Ultimately, the potential to determine solid phase half saturation constants at different flow rates makes this approach appealing and encourages further development despite its limitations.

CHAPTER 5: CONCLUSIONS AND FUTURE WORK

This study suggests that a solid phase half saturation constant may be estimated using a flow through system amended with solid phase electron acceptor, and that the half saturation constant may be influenced by the average linear velocity through the system. It can also be inferred from the data presented in previous sections that the formation of colonies within a biofilm may be correlated with the point in time where maximum reduction is occurring. Future experiments are needed to make a stronger comparison of morphology to reduction kinetics.

In future experiments, it will be important to collect more accurate data. In the first three experiments, the maximum rate of manganese reduction may have been missed due to sampling frequency. Based on recent high flow rate data, sampling every twelve hours gives a more complete representation of the manganese reduction in the system (Figure 2). It will also be important to improve the protein assay methods to obtain better estimates of biomass. The method described for the protein assay resulted in protein concentrations very close to or below the detection limit, which is approximately 1 μg/mL. This likely caused imprecise measurements with considerable error. In future experiments, this approach for estimating cell count could be improved by using a smaller volume of media when removing biomass from the glass slides. The protein would be more concentrated in solution and allow for a more precise measurement. Additionally, multiple extractions from the same solution should be done to accurately evaluate the error involved in the extraction method.

Improvements to the mass balance could be made by measuring the initial mass of MnO_2 on a microscale to improve accuracy. Measuring accurately to the $10{,}000^{th}$ of a gram would likely bring the mass balance closer to 100%. The amount of water should also be accounted for with each MnO_2 coating. Three slides not used in the experiment, but coated at the same time as those being used, should be dried in a 105°C oven for 24 hours and then massed again on the microscale to estimate the percentage of water lost from the slides.

It would also be beneficial to obtain a better estimate of initial biomass. This can be done by measuring the effluent on the ICP daily to determine when the manganese reduction rate begins to increase. On the first day that the effluent manganese concentration exceeds 0.05 ppm, the first slide should be removed. This first slide will be used to get an approximation for initial biomass because it will have been removed from the reactor before the biomass reaches the exponential growth phase.

With improved data collection, the model may still have difficulty obtaining a perfect fit for late time experimental data. This may be due to neglecting to account for electron transport from the solid phase electron acceptor through the biofilm. A Nernst-Monod model could be helpful in mitigating any

discrepancies between the simple Monod model presented above and the experimental data (Picioreanu et al., 2007; Torres et al., 2010; Torres et al., 2008). Literature related to microbial fuel cells could be useful in modeling the reduction of solid phase MnO_2.

Based on the data presented, future experiments should include three experiments at three different flow rates (high, medium, and low) to account for natural variation within one flow rate. All nine experiments should aim to have approximately the same mass of MnO_2 initially introduced into the system. Control experiments should also be conducted without inoculum and with a very low flow. The lack of inoculum will prove that biological reduction is the only mechanism contributing to MnO_2 reduction, and the very low flow experiment will give a baseline for the morphology of bacteria expected when shear from the flow is not impacting the growth of the biofilm.

REFERENCES

Anderson, R. T., Vrionis, H. A., Ortiz-Bernad, I., Resch, C. T., Long, P. E., Dayvault, R., … Lovley, D. R. (2003). Stimulating the in situ activity of Geobacter species to remove uranium from the groundwater of a uranium-contaminated aquifer. *Applied and Environmental Microbiology*, *69*(10), 5884–5891.

Bethke, C. M., Sanford, R. A., Kirk, M. F., Jin, Q., & Flynn, T. M. (2011). The thermodynamic ladder in geomicrobiology. *American Journal of Science*, *311*(3), 183–210. http://doi.org/10.2475/03.2011.01

Brown, D. G., Komlos, J., & Jaffé, P. R. (2005). Simultaneous Utilization of Acetate and Hydrogen by Geobacter sulfurreducens and Implications for Use of Hydrogen as an Indicator of Redox Conditions. *Environmental Science & Technology*, *39*(9), 3069–3076. http://doi.org/10.1021/es048613p

Costerton, J. W., Lewandowski, Z., Caldwell, D. E., Korber, D. R., & Lappin-Scott, H. M. (1995). Microbial Biofilms. *Annual Review of Microbiology*, *49*(1), 711–745. http://doi.org/10.1146/annurev.mi.49.100195.003431

Fang, Y., Yabusaki, S. B., Morrison, S. J., Amonette, J. P., & Long, P. E. (2009). Multicomponent reactive transport modeling of uranium bioremediation field experiments. *Geochimica et Cosmochimica Acta*, *73*(20), 6029–6051. http://doi.org/10.1016/j.gca.2009.07.019

Hall-Stoodley, L., Costerton, J. W., & Stoodley, P. (2004). Bacterial biofilms: from the Natural environment to infectious diseases. *Nature Reviews Microbiology*, *2*(2), 95–108. http://doi.org/10.1038/nrmicro821

Henze, M. (2008). *Biological Wastewater Treatment: Principles, Modelling and Design*. IWA Publishing.

Holmes, D. E., Giloteaux, L., Barlett, M., Chavan, M. A., Smith, J. A., Williams, K. H., … Lovley, D. R. (2013). Molecular Analysis of the In Situ Growth Rates of Subsurface Geobacter Species. *Applied and Environmental Microbiology*, *79*(5), 1646–1653. http://doi.org/10.1128/AEM.03263-12

Holtan-Hartwig, L., Dörsch, P., & Bakken, L. R. (2000). Comparison of denitrifying communities in organic soils: kinetics of NO−3 and N2O reduction. *Soil Biology and Biochemistry*, *32*(6), 833–843. http://doi.org/10.1016/S0038-0717(99)00213-8

Homoncik, S. C., MacDonald, A. M., Heal, K. V., Ó Dochartaigh, B. É., & Ngwenya, B. T. (2010). Manganese concentrations in Scottish groundwater. *Science of The Total Environment*, *408*(12), 2467–2473. http://doi.org/10.1016/j.scitotenv.2010.02.017

Istok, J. D., Senko, J. M., Krumholz, L. R., Watson, D., Bogle, M. A., Peacock, A., … White, D. C. (2004). In Situ Bioreduction of Technetium and Uranium in a Nitrate-Contaminated Aquifer. *Environmental Science & Technology*, *38*(2), 468–475. http://doi.org/10.1021/es034639p

Korber, D. R., Lawrence, J. R., Sutton, B., & Caldwell, D. E. (1989). Effect of laminar flow velocity on the kinetics of surface recolonization by Mot+ and Mot− Pseudomonas fluorescens. *Microbial Ecology*, *18*(1), 1–19. http://doi.org/10.1007/BF02011692

Li, L., Steefel, C. I., Williams, K. H., Wilkins, M. J., & Hubbard, S. S. (2009). Mineral Transformation and Biomass Accumulation Associated With Uranium Bioremediation at Rifle, Colorado. *Environmental Science & Technology*, *43*(14), 5429–5435. http://doi.org/10.1021/es900016v

Li, P., Qian, H., Howard, K. W. F., Wu, J., & Lyu, X. (2013). Anthropogenic pollution and variability of manganese in alluvial sediments of the Yellow River, Ningxia, northwest China. *Environmental Monitoring and Assessment*, *186*(3), 1385–1398. http://doi.org/10.1007/s10661-013-3461-3

Liu, C., Gorby, Y. A., Zachara, J. M., Fredrickson, J. K., & Brown, C. F. (2002). Reduction kinetics of Fe(III), Co(III), U(VI), Cr(VI), and Tc(VII) in cultures of dissimilatory metal-reducing bacteria. *Biotechnology and Bioengineering*, *80*(6), 637–649. http://doi.org/10.1002/bit.10430

Lovley, D. D. (2013). Dissimilatory Fe(III)- and Mn(IV)-Reducing Prokaryotes. In E. Rosenberg, E. F. DeLong, S. Lory, E. Stackebrandt, & F. Thompson (Eds.), *The Prokaryotes* (pp. 287–308). Springer Berlin Heidelberg. Retrieved from http://link.springer.com/referenceworkentry/10.1007/978-3-642-30141-4_69

Lovley, D. R. (1993). Dissimilatory Metal Reduction. *Annual Review of Microbiology*, *47*(1), 263–290. http://doi.org/10.1146/annurev.mi.47.100193.001403

Lovley, D. R. (2002). Dissimilatory metal reduction: from early life to bioremediation. *Asm News*, *68*(5), 231–237.

Lovley, D. R., & Phillips, E. J. P. (1988). Novel Mode of Microbial Energy Metabolism: Organic Carbon Oxidation Coupled to Dissimilatory Reduction of Iron or Manganese. *Applied and Environmental Microbiology*, *54*(6), 1472–1480.

Madigan, M. T., Clark, D. P., Stahl, D., & Martinko, J. M. (2010). *Brock Biology of Microorganisms 13th Edition*. Benjamin Cummings.

Makkar, H. P. S., Sharma, O. P., Dawra, R. K., & Negi, S. S. (1982). Simple Determination of Microbial Protein in Rumen Liquor. *Journal of Dairy Science*, *65*(11), 2170–2173. http://doi.org/10.3168/jds.S0022-0302(82)82477-6

Messerli, M. (1993). *IMARIS*. Zurich, Switzerland: Bitplane.

Mulder, C., & Hendriks, A. J. (2014). Half-saturation constants in functional responses. *Global Ecology and Conservation*, *2*, 161–169. http://doi.org/10.1016/j.gecco.2014.09.006

Picioreanu, C. (2000). Effect of diffusive and convective substrate transport on biofilm structure formation: A two-dimensional modeling study. *Biotechnology and Bioengineering*, *69*(5), 504–15. http://doi.org/10.1002/1097-0290(20000905)69:53.0.CO;2-S

Picioreanu, C., Head, I. M., Katuri, K. P., van Loosdrecht, M. C. M., & Scott, K. (2007). A computational model for biofilm-based microbial fuel cells. *Water Research*, *41*(13), 2921–2940. http://doi.org/10.1016/j.watres.2007.04.009

Post, J. E. (1999). Manganese oxide minerals: Crystal structures and economic and environmental significance. *Proceedings of the National Academy of Sciences*, *96*(7), 3447–3454. http://doi.org/10.1073/pnas.96.7.3447

Purevdorj, B., Costerton, J. W., & Stoodley, P. (2002). Influence of Hydrodynamics and Cell Signaling on the Structure and Behavior of Pseudomonas aeruginosa Biofilms. *Applied and Environmental Microbiology*, *68*(9), 4457–4464. http://doi.org/10.1128/AEM.68.9.4457-4464.2002

Rasband, W. S. (1997). *ImageJ*. Bethesda, Maryland: U. S. National Institutes of Health. Retrieved from http://imagej.nih.gov/ij/

Rittmann, B. E. (2001). *Environmental Biotechnology: Principles and Applications. Bruce E. Rittmann, Perry L. McCarty*. Boston: McGraw-Hill.

Roden, E. E. (2006). Geochemical and microbiological controls on dissimilatory iron reduction. *Comptes Rendus Geoscience*, *338*(6–7), 456–467. http://doi.org/10.1016/j.crte.2006.04.009

Roden, E. E., & Jin, Q. (2011). Thermodynamics of Microbial Growth Coupled to Metabolism of Glucose, Ethanol, Short-Chain Organic Acids, and Hydrogen. *Applied and Environmental Microbiology*, *77*(5), 1907–1909. http://doi.org/10.1128/AEM.02425-10

Roden, E. E., & Zachara, J. M. (1996). Microbial Reduction of Crystalline Iron(III) Oxides: Influence of Oxide Surface Area and Potential for Cell Growth. *Environmental Science & Technology*, *30*(5), 1618–1628. http://doi.org/10.1021/es9506216

Stoodley, P., Cargo, R., Rupp, C. J., Wilson, S., & Klapper, I. (2002). Biofilm material properties as related to shear-induced deformation and detachment phenomena. *Journal of Industrial Microbiology and Biotechnology*, *29*(6), 361–367. http://doi.org/10.1038/sj.jim.7000282

Tebo, B. M., Bargar, J. R., Clement, B. G., Dick, G. J., Murray, K. J., Parker, D., … Webb, S. M. (2004). Biogenic Manganese Oxides: Properties and Mechanisms of Formation. *Annual Review of Earth and Planetary Sciences*, *32*(1), 287–328. http://doi.org/10.1146/annurev.earth.32.101802.120213

Torres, C. I., Marcus, A. K., Lee, H.-S., Parameswaran, P., Krajmalnik-Brown, R., & Rittmann, B. E. (2010). A kinetic perspective on extracellular electron transfer by anode-respiring bacteria. *FEMS Microbiology Reviews*, *34*(1), 3–17. http://doi.org/10.1111/j.1574-6976.2009.00191.x

Torres, C. I., Marcus, A. K., Parameswaran, P., & Rittmann, B. E. (2008). Kinetic Experiments for Evaluating the Nernst−Monod Model for Anode-Respiring Bacteria (ARB) in a Biofilm Anode. *Environmental Science & Technology*, *42*(17), 6593–6597. http://doi.org/10.1021/es800970w

Truex, M. J., Peyton, B. M., Valentine, N. B., & Gorby, Y. A. (1997). Kinetics of U(VI) reduction by a dissimilatory Fe(III)-reducing bacterium under non-growth conditions. *Biotechnology and Bioengineering*, *55*(3), 490–496. http://doi.org/10.1002/(SICI)1097-0290(19970805)55:3<490::AID-BIT4>3.0.CO;2-7

Villalobos, M., Toner, B., Bargar, J., & Sposito, G. (2003). Characterization of the manganese oxide produced by pseudomonas putida strain MnB1. *Geochimica et Cosmochimica Acta*, *67*(14), 2649–2662. http://doi.org/10.1016/S0016-7037(03)00217-5

Williams, B. A., Brown, C. F., Um, W., Nimmons, M. J., Peterson, R. E., Bjornstad, B. N., … Rockhold, M. L. (2007). *Limited Field Investigation Report for Uranium Contamination in the 300 Area, 300-FF-5 Operable Unit, Hanford Site, Washington* (Technical Report No. PNNL-16435). Richland, WA: Pacific Northwest National Laboratory (PNNL).

Wu, W.-M., Carley, J., Gentry, T., Ginder-Vogel, M. A., Fienen, M., Mehlhorn, T., … Criddle, C. S. (2006). Pilot-Scale in Situ Bioremedation of Uranium in a Highly Contaminated Aquifer. 2. Reduction of U(VI) and Geochemical Control of U(VI) Bioavailability. *Environmental Science & Technology*, *40*(12), 3986–3995. http://doi.org/10.1021/es051960u

Yabusaki, S. B., Fang, Y., Long, P. E., Resch, C. T., Peacock, A. D., Komlos, J., … Anderson, R. T. (2007). Uranium removal from groundwater via in situ biostimulation: Field-scale modeling of transport and biological processes. *Journal of Contaminant Hydrology*, *93*(1–4), 216–235. http://doi.org/10.1016/j.jconhyd.2007.02.005

Zhong, L., Liu, C., Zachara, J. M., Kennedy, D. W., Szecsody, J. E., & Wood, B. (2005). Oxidative remobilization of biogenic uranium(IV) precipitates : Effects of iron(II) and pH. *Journal of Environmental Quality*, *34*(5), 1763–1771.

APPENDIX A: LARGE TABLES

Table A.1. Media components.

Mineral Solution (x10)	*Stock Conc. (g/L)*	*Final Conc. (mM)*
NH_4Cl	2.675	5
KH_2PO_4	0.544	0.4
$MgCl_2 \cdot 6H_2O$	2.04	1
$CaCl_2 \cdot 6H_2O$	1.47	1
Trace Elements Solution (x1000)	*Stock Conc. (g/L)*	*Final Conc. (nM)*
$FeCl_2$ (in 10 mL 25% HCl)	1.27	10000
$CoCl_2$	0.13	1000
$MnCl_2 \cdot 4H_2O$	0.198	1000
$ZnCl_2$	0.136	1000
H_3BO_3	0.0062	100
$NiCl_2$	0.013	100
$AlCl_3$	0.0133	100
$Na_2MoO_4 \cdot 2H_2O$	0.0242	100
Se/W Solution (x1000)	*Stock Conc. (g/L)*	*Final Conc. (nM)*
Na_2SeO_3	0.0017	10
$Na_2WO_4 \cdot 2H_2O$	0.0033	10
Vitamins Solution (x1000)	*Stock Conc. (mg/L)*	
Biotin	5	
p-ABA (p-aminobenzoic acid)	5	
Pantothenate (Ca salt)	5	
Pyridoxine-HCl	10	
Nicotinic acid	5	
Thiamine-HCl $\cdot 2H_2O$	5	
Lipoic acid (Thioctic acid)	5	
Folic acid	5	
B_{12}	5	
Riboflavin	5	

Table A.2. Calculate parameters from manganese effluent and image and protein assay cell estimates. Strikethrough indicates IMARIS image data not used to calculate yield and μ_{max}.

Experiment 2					
Day	Cell Count from IMARIS Images	Cell Count from Protein Assay	Cumulative Manganese Effluent (moles MnO_2)	Yield (cells/mmol MnO_2)	μ_{max} (1/hr)
8	2.65E+08		2.37E-07		
10			4.69E-07		
11			1.31E-06		
14	~~2.34E+08~~	3.95E+08	4.99E-06	2.73E+10	0.0027
16		1.10E+09	1.52E-05	6.86E+10	**0.0196**
18			2.25E-05		
20		1.23E+09	2.56E-05	1.26E+10	0.0012
22	~~4.03E+08~~	1.30E+09	2.85E-05	2.41E+10	0.0056
Experiment 3					
Day	Cell Count from IMARIS Images	Cell Count from Protein Assay	Cumulative Manganese Effluent (moles)	Yield (cells/mmol)	u_max (1/hr)
9	1.47E+08		1.36E-07		
11			9.92E-07		
13		1.00E+09	1.19E-05	7.25E+10	**0.0155**
14	~~4.04E+08~~	8.87E+08	1.94E-05	negative	0.0119
16		7.77E+08	2.81E-05	negative	Negative
18		1.18E+09	3.29E-05	8.49E+10	0.0086
20	~~1.50E+09~~	1.25E+09	3.63E-05	1.93E+10	0.0024
Experiment 4					
Day	Cell Count from IMARIS Images	Cell Count from Trendline	Cumulative Manganese Effluent (moles)	Yield (cells/mmol)	u_max (1/hr)
9	7.73E+07	2.72E+08	7.509E-07	-	
11	1.07E+09	6.35E+08	7.556E-06	5.34E+10	**0.0167**
12	5.64E+08	7.88E+08	2.693E-05	7.89E+09	0.0090
13	1.02E+09	9.22E+08	3.688E-05	1.35E+10	0.0065
15	1.18E+09	1.13E+09	4.295E-05	3.46E+10	0.0043
17	9.09E+08	1.27E+09	5.022E-05	1.84E+10	0.0023
19	1.52E+09	1.32E+09	5.564E-05	1.05E+10	0.0009

APPENDIX B: RAW DATA

Table B.1. Manganese effluent data.

Experiment 1: No Slide Removal at 5 mL/hr									
Sample Date	Days Since Inoculation	Concentration (mg/L)	Volume of Effluent (mL)	Mass in Effluent (mmol)	Slides Removed	Mass to Add for Missing Slides (mmol)	Total Mass All Slides Present (mmol)	Total Mass One Slide Present (mmol)	Cummulative Mass One Slide Present (mmol)
8/23/2014	0	0.236	160	6.87E-04	0	0	6.87E-04	9.82E-05	9.82E-05
8/26/2014	1	0.468	422	3.59E-03	0	0	3.59E-03	5.14E-04	6.12E-04
8/28/2014	3	0.292	418	2.22E-03	0	0	2.22E-03	3.17E-04	9.29E-04
8/30/2014	5	0.236	422	1.81E-03	0	0	1.81E-03	2.59E-04	1.19E-03
9/1/2014	7	1.156	421	8.86E-03	0	0	8.86E-03	1.27E-03	2.45E-03
9/3/2014	9	7.8	448	6.36E-02	0	0	6.36E-02	9.09E-03	1.15E-02
9/5/2014	11	7.5	463	6.32E-02	0	0	6.32E-02	9.03E-03	2.06E-02
9/8/2014	14	4.5	454	3.72E-02	0	0	3.72E-02	5.31E-03	2.59E-02

Experiment 2: Slide Removal at 5 mL/hr									
Sample Date	Days Since Inoculation	Concentration (mg/L)	Volume of Effluent (mL)	Mass in Effluent (mmol)	Slides Removed	Mass to Add for Missing Slides (mmol)	Total Mass All Slides Present (mmol)	Total Mass One Slide Present (mmol)	Cummulative Mass One Slide Present (mmol)
9/30/2014	1	0.047	457	3.91E-04	0	0	3.91E-04	5.59E-05	5.59E-05
10/2/2014	3	0.038	458	3.17E-04	0	0	3.17E-04	4.53E-05	1.01E-04
10/3/2014	4	0.036	360	2.36E-04	0	0	2.36E-04	3.37E-05	1.35E-04
10/5/2014	6	0.045	462	3.78E-04	0	0	3.78E-04	5.41E-05	1.89E-04
10/7/2014	8	0.036	443	2.90E-04	1	4.84E-05	3.39E-04	4.84E-05	2.37E-04
10/9/2014	10	0.14	455	1.16E-03	2	4.64E-04	1.62E-03	2.32E-04	4.69E-04
10/10/2014	11	0.54	344	3.38E-03	3	2.54E-03	5.92E-03	8.45E-04	1.31E-03
10/12/2014	13	1.78	454	1.47E-02	3	1.10E-02	2.57E-02	3.68E-03	4.99E-03
10/15/2014	16	3.82	441	3.07E-02	4	4.09E-02	7.15E-02	1.02E-02	1.52E-02
10/17/2014	18	1.78	451	1.46E-02	5	3.65E-02	5.11E-02	7.31E-03	2.25E-02
10/19/2014	20	0.75	455	6.21E-03	5	1.55E-02	2.17E-02	3.11E-03	2.56E-02
10/21/2014	22	0.36	442	2.90E-03	6	1.74E-02	2.03E-02	2.90E-03	2.85E-02

Experiment 3: Slide Removal at 5 mL/hr									
Sample Date	Days Since Inoculation	Concentration (mg/L)	Volume of Effluent (mL)	Mass in Effluent (mmol)	Slides Removed	Mass to Add for Missing Slides (mmol)	Total Mass All Slides Present (mmol)	Total Mass One Slide Present (mmol)	Cummulative Mass One Slide Present (mmol)
10/30/2014	0	0.032	361	2.10E-04	0	0	2.10E-04	3.00E-05	3.00E-05
11/1/2014	1	0.03	459	2.51E-04	0	0	2.51E-04	3.58E-05	6.58E-05
11/3/2014	3	0.022	446	1.79E-04	0	0	1.79E-04	2.55E-05	9.14E-05
11/5/2014	5	0.022	448	1.79E-04	0	0	1.79E-04	2.56E-05	1.17E-04
11/7/2014	7	0.022	461	1.85E-04	0	0	1.85E-04	2.64E-05	1.43E-04
11/9/2014	9	0.02	427	1.55E-04	0	0	1.55E-04	2.22E-05	1.66E-04
11/11/2014	11	0.66	428	5.14E-03	1	8.57E-04	6.00E-03	8.57E-04	1.02E-03
11/13/2014	13	8.28	436	6.57E-02	1	1.10E-02	7.67E-02	1.10E-02	1.20E-02
11/14/2014	14	6.2	330	3.72E-02	2	1.49E-02	5.21E-02	7.45E-03	1.94E-02
11/16/2014	16	4.34	441	3.48E-02	3	2.61E-02	6.10E-02	8.71E-03	2.81E-02
11/18/2014	18	1.82	433	1.43E-02	4	1.91E-02	3.35E-02	4.78E-03	3.29E-02
11/20/2014	20	0.84	444	6.79E-03	5	1.70E-02	2.38E-02	3.39E-03	3.63E-02

Table B.1. (Continued) Manganese effluent data.

Experiment 4: Slide Removal at 5 mL/hr									
Sample Date	Days Since Inoculation	Concentration (mg/L)	Volume of Effluent (mL)	Mass in Effluent (mmol)	Slides Removed	Mass to Add for Missing Slides (mmol)	Total Mass All Slides Present (mmol)	Total Mass One Slide Present (mmol)	Cummulative Mass One Slide Present (mmol)
3/25/2015	0	0.04	363	2.93E-04	0	0	2.93E-04	4.19E-05	4.19E-05
3/27/2015	0	0.05	451	3.94E-04	0	0	3.94E-04	5.63E-05	9.83E-05
3/29/2015	2	0.04	454	3.27E-04	0	0	3.27E-04	4.68E-05	1.45E-04
3/31/2015	4	0.03	464	2.13E-04	0	0	2.13E-04	3.05E-05	1.76E-04
4/2/2015	6	0.03	464	2.62E-04	0	0	2.62E-04	3.74E-05	2.13E-04
4/4/2015	8	0.45	459	3.77E-03	0	0	3.77E-03	5.38E-04	7.51E-04
4/6/2015	10	4.84	463	4.08E-02	1	6.80E-03	4.76E-02	6.80E-03	7.56E-03
4/7/2015	11	6.76	359	4.42E-02	2	1.77E-02	6.19E-02	8.84E-03	1.64E-02
4/8/2015	12	10.48	221	4.22E-02	3	3.16E-02	7.38E-02	1.05E-02	2.69E-02
4/9/2015	13	6.86	239	2.98E-02	4	3.98E-02	6.96E-02	9.94E-03	3.69E-02
4/10/2015	14	4.53	221	1.82E-02	4	2.43E-02	4.25E-02	6.07E-03	4.29E-02
4/12/2015	16	2.68	298	1.45E-02	5	3.64E-02	5.09E-02	7.27E-03	5.02E-02
4/14/2015	18	0.64	462	5.42E-03	6	3.25E-02	3.80E-02	5.42E-03	5.56E-02

Experiment 5: Slide Removal at 50 mL/hr									
Sample Date	Days Since Inoculation	Concentration (mg/L)	Volume of Effluent (mL)	Mass in Effluent (mmol)	Slides Removed	Mass to Add for Missing Slides (mmol)	Total Mass All Slides Present (mmol)	Total Mass One Slide Present (mmol)	Cummulative Mass One Slide Present (mmol)
6/8/15 15:00	0.00	0	0	0.00E+00	0	0	0.00E+00	0.00E+00	0.00E+00
6/9/15 14:10	1.00	0.127597705	217	5.04E-04	0	0	5.04E-04	7.20E-05	7.20E-05
6/9/15 16:10	1.08	0.122401815	237	5.28E-04	0	0	5.28E-04	7.54E-05	1.47E-04
6/10/15 8:45	1.75	0.087302049	795	1.26E-03	0	0	1.26E-03	1.80E-04	3.28E-04
6/11/15 0:00	2.42	0.089055895	682	1.11E-03	0	0	1.11E-03	1.58E-04	4.86E-04
6/11/15 19:20	3.21	0.16375446	855	2.55E-03	0	0	2.55E-03	3.64E-04	8.50E-04
6/12/15 11:45	3.92	0.42082606	760	5.82E-03	0	0	5.82E-03	8.32E-04	1.68E-03
6/12/15 22:45	4.38	0.760984343	520	7.20E-03	0	0	7.20E-03	1.03E-03	2.71E-03
6/13/15 12:00	4.88	1.429046925	635	1.65E-02	0	0	1.65E-02	2.36E-03	5.07E-03
6/14/15 7:00	5.67	4.316924825	845	6.64E-02	0	0	6.64E-02	9.49E-03	1.46E-02
6/14/15 23:00	6.33	7.899216825	705	1.01E-01	0	0	1.01E-01	1.45E-02	2.90E-02
6/15/15 11:30	6.85	7.729408575	590	8.30E-02	0	0	8.30E-02	1.19E-02	4.09E-02
6/15/15 22:15	7.30	5.05002835	525	4.83E-02	1	8.04E-03	5.63E-02	8.04E-03	4.89E-02
6/16/15 10:45	7.79	2.75309435	610	3.06E-02	1	5.09E-03	3.57E-02	5.09E-03	5.40E-02
6/16/15 22:30	8.29	1.29578335	565	1.33E-02	2	5.33E-03	1.87E-02	2.67E-03	5.67E-02
6/17/15 10:30	8.81	0.528489713	580	5.58E-03	2	2.23E-03	7.81E-03	1.12E-03	5.78E-02
6/17/15 21:30	9.27	0.254372945	510	2.36E-03	3	1.77E-03	4.13E-03	5.90E-04	5.84E-02
6/18/15 9:00	9.75	0.15058383	550	1.51E-03	3	1.13E-03	2.64E-03	3.77E-04	5.88E-02
6/18/15 21:00	10.13	0.228732925	550	2.29E-03	4	3.05E-03	5.34E-03	7.63E-04	5.95E-02
6/19/15 10:30	10.69	0.095613888	650	1.13E-03	4	1.51E-03	2.64E-03	3.77E-04	5.99E-02

Table B.2. Water content in manganese dioxide.

Slide	Slide Mass Initial (g)	Mass after Coating and Air Dry (g)	Mass after Oven Dry (g)	MnO_2 estimated After Air Dry (g)	MnO_2 actual After Oven Dry (g)	Difference (Estimated - Actual)	Percent Water
A	4.4947	4.5002	4.4998	0.0055	0.0051	0.0004	7.27%
B	4.4859	4.4915	4.4910	0.0056	0.0051	0.0005	8.93%
C	4.5887	4.5947	4.5942	0.0060	0.0055	0.0005	8.33%
D	4.5761	4.5825	4.5818	0.0064	0.0057	0.0007	10.94%
E	4.4606	4.4645	4.4640	0.0039	0.0034	0.0005	12.82%
F	4.4858	4.4922	4.4917	0.0064	0.0059	0.0005	7.81%
G	4.3959	4.4023	4.4018	0.0064	0.0059	0.0005	7.81%
H	4.4557	4.4587	4.4585	0.0030	0.0028	0.0002	6.67%
						Average Percent:	8.82%

Figure B.1. Water content per initial mass of manganese dioxide coated.

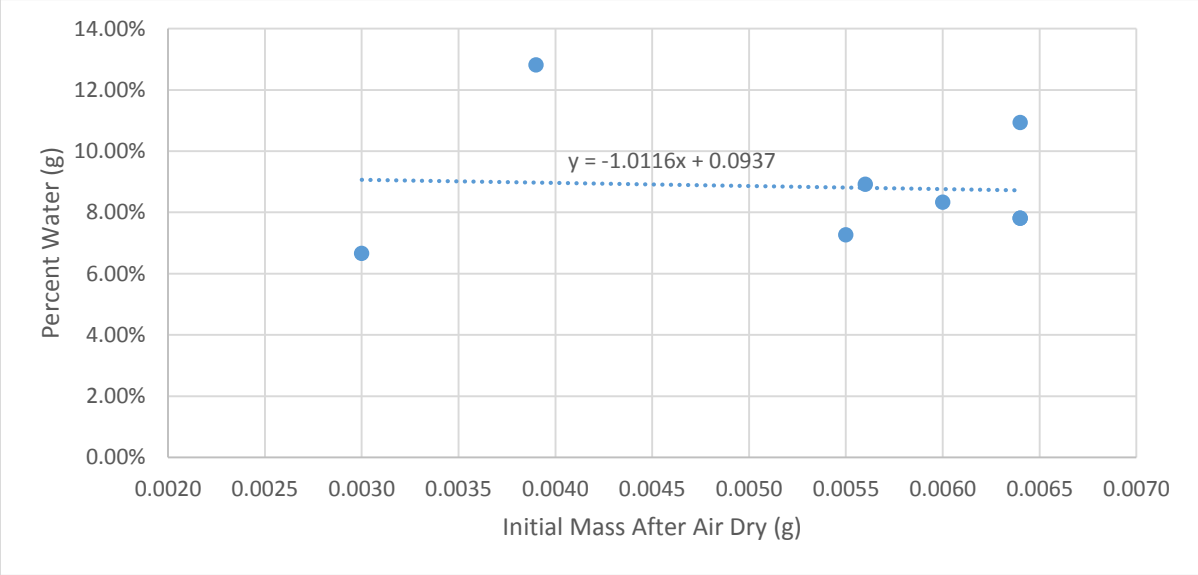

Table B.3. Standards for protein assay.

Standards		
Concentration (ug/mL)	Absorbance	Corrected Absorbance
20	1.0181	0.6321
15	0.8989	0.5129
10	0.7345	0.3485
5	0.6319	0.2459
2	0.492	0.106
1	0.4705	0.0845
0	0.386	0

Figure B.2. Protein assay data.

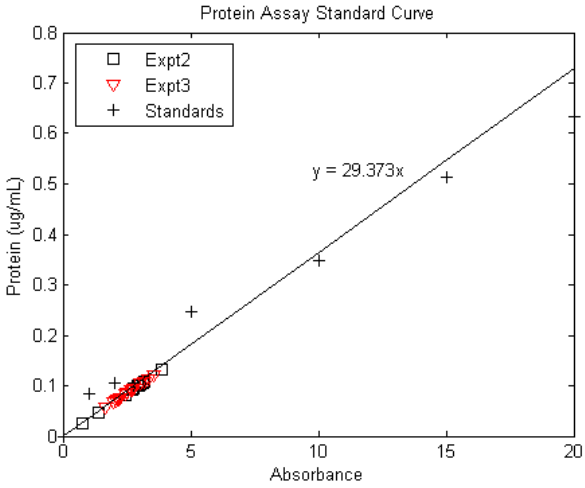

Table B.4. Protein assay data for Experiment 2.

Experiment 2 Protein Assay									
Sample	Absorbance	Corrected Absorbance	Protein Concentration (µg/mL)	Mass in 2 mL Subsample (µg)	Volume of Solution (mL)	Total Mass (µg)	Average Mass (µg)	**Geobacter Count (cells)**	**Standard Deviation (cells)**
Day 6 - A	0.3440	-0.0420							
Day 6 - B	0.3632	-0.0228							
Day 6 - C	0.3495	-0.0365							
Day 8 - A	0.3385	-0.0475							
Day 8 - B	0.3241	-0.0619							
Day 8 - C	0.3303	-0.0557							
Day 10 - A	0.3398	-0.0462							
Day 10 - B	0.3230	-0.0630							
Day 10 - C	0.3153	-0.0707							
Day 14 - A	0.4333	0.0473	1.39	2.78	40	55.57			
Day 14 - B	0.4123	0.0263	0.77	1.55	40	30.90	39.01	3.90E+08	1.43E+08
Day 14 - C	0.4120	0.0260	0.76	1.53	40	30.55			
Day 16 - A	0.4880	0.1020	3.00	5.99	40	119.84			
Day 16 - B	0.4777	0.0917	2.69	5.39	40	107.74	108.17	1.08E+09	1.15E+08
Day 16 - C	0.4685	0.0825	2.42	4.85	40	96.93			
Day 20 - A	0.4922	0.1062	3.12	6.24	40	124.78			
Day 20 - B	0.4953	0.1093	3.21	6.42	40	128.42	121.10	1.21E+09	9.70E+07
Day 20 - C	0.4797	0.0937	2.75	5.50	40	110.09			
Day 22 - A	0.5179	0.1319	3.87	7.75	40	154.97			
Day 22 - B	0.4861	0.1001	2.94	5.88	40	117.61	127.98	1.28E+09	1.80E+08
Day 22 - C	0.4887	0.1027	3.02	6.03	40	120.66			
Day 22 - D	0.4870	0.1010	2.97	5.93	40	118.67			

Table B.5. Protein assay data for Experiment 3.

Experiment 3 Protein Assay									
Sample	Absorbance	Corrected Absorbance	Protein Concentration (µg/mL)	Mass in 2 mL Subsample (µg)	Volume of Solution (mL)	Total Mass (µg)	Average Mass (µg)	**Geobacter Count (cells)**	**Standard Deviation (cells)**
Day 9 - A	0.2580	-0.1280							
Day 9 - B	0.2393	-0.1467							
Day 9 - C	0.2495	-0.1365							
Day 13 - A	0.4716	0.0856	2.51	5.01	40	100.23			
Day 13 - B	0.4703	0.0843	2.47	4.94	40	98.71	98.67	9.87E+08	1.58E+07
Day 13 - C	0.4689	0.0829	2.43	4.85	40	97.07			
Day 14 - A	0.4598	0.0738	2.16	4.32	40	86.41			
Day 14 - B	0.4593	0.0733	2.15	4.29	40	85.83	87.19	8.72E+08	1.88E+07
Day 14 - C	0.4623	0.0763	2.23	4.47	40	89.34			
Day 16 - A	0.4537	0.0677	1.98	3.96	40	79.27			
Day 16 - B	0.4566	0.0706	2.07	4.13	40	82.67	76.42	7.64E+08	8.06E+07
Day 16 - C	0.4435	0.0575	1.68	3.37	40	67.33			
Day 18 - A	0.4773	0.0913	2.67	5.35	40	106.90			
Day 18 - B	0.4788	0.0928	2.72	5.43	40	108.66	116.35	1.16E+09	1.49E+08
Day 18 - C	0.5000	0.1140	3.34	6.67	40	133.48			
Day 20a - A	0.5074	0.1214	3.55	7.11	40	142.15			
Day 20a - B	0.4947	0.1087	3.18	6.36	40	127.28	126.38	1.26E+09	1.62E+08
Day 20a - C	0.4797	0.0937	2.74	5.49	40	109.72			
Day 20b - A	0.4793	0.0933	2.73	5.46	40	109.25			
Day 20b - B	0.4939	0.1079	3.16	6.32	40	126.34	119.20	1.19E+09	8.89E+07
Day 20b - C	0.4902	0.1042	3.05	6.10	40	122.01			

APPENDIX C: CONFOCAL IMAGES AND IMAGE ANALYSIS

Figure C.1. Confocal Images from the second and third experiments.

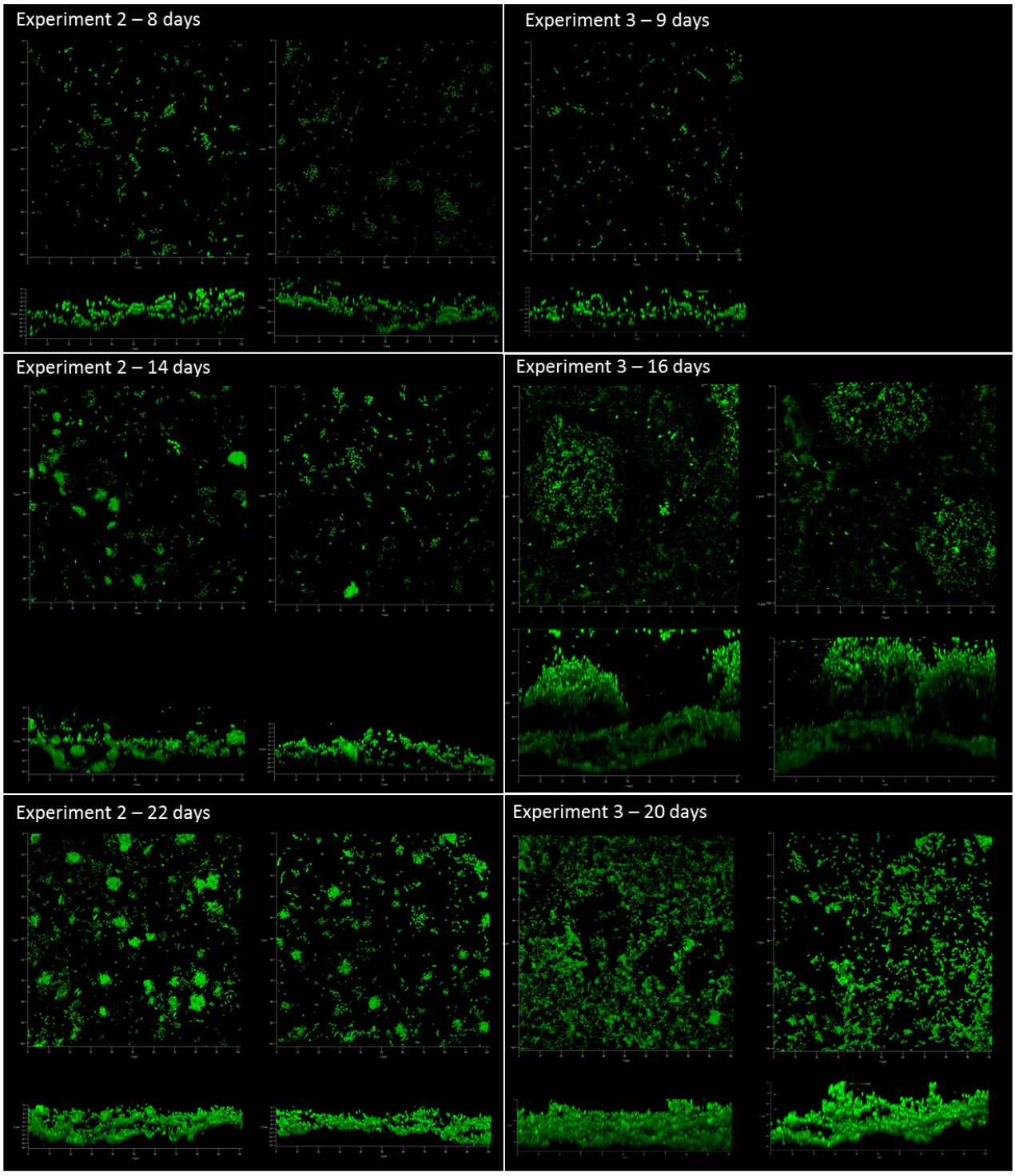

Figure C.2. Confocal images from the fourth experiment.

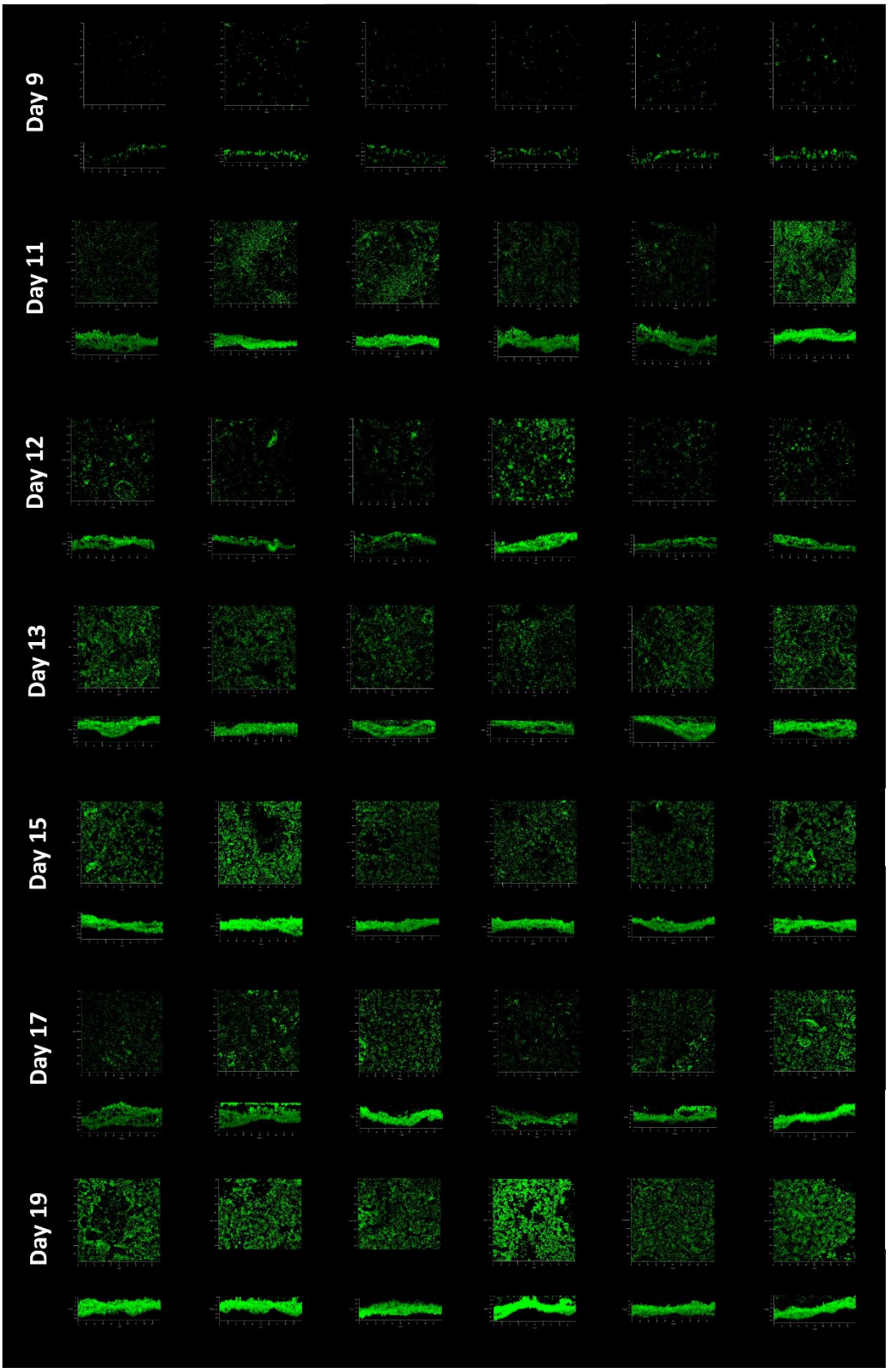

Figure C.3. ImageJ projections of Experiment 2 confocal images.

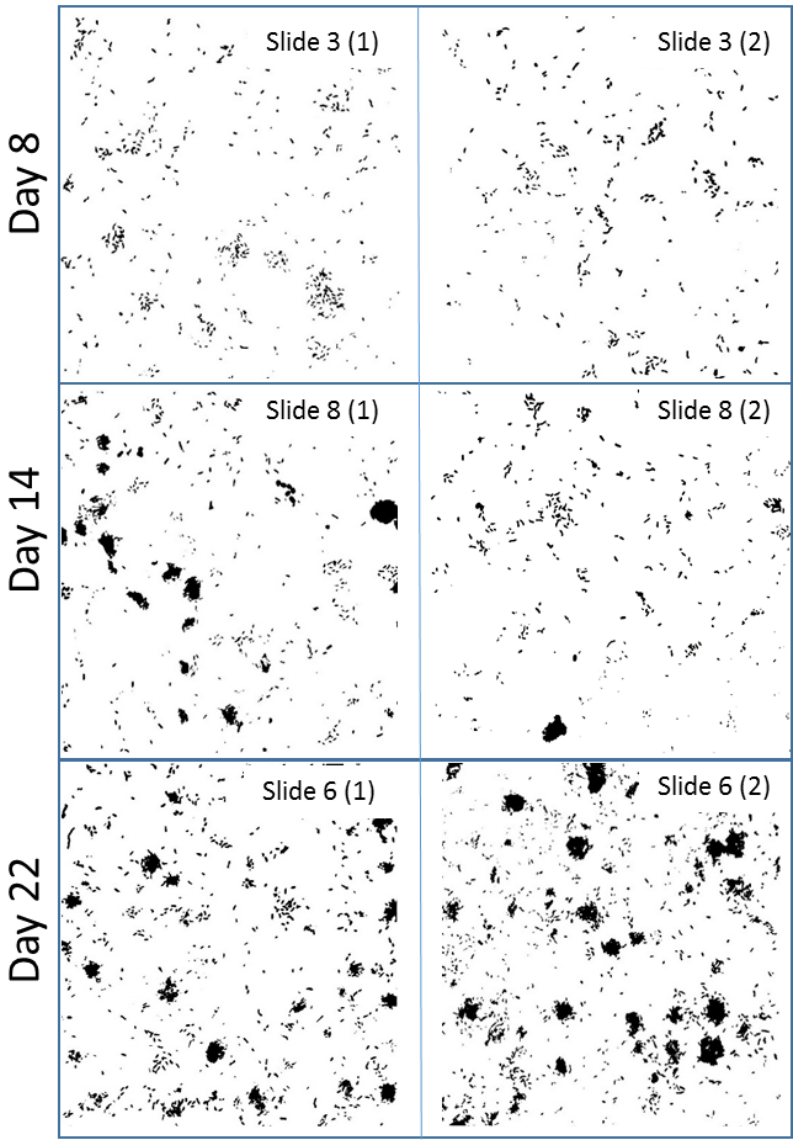

Figure C.4. ImageJ projections of Experiment 3 confocal images.

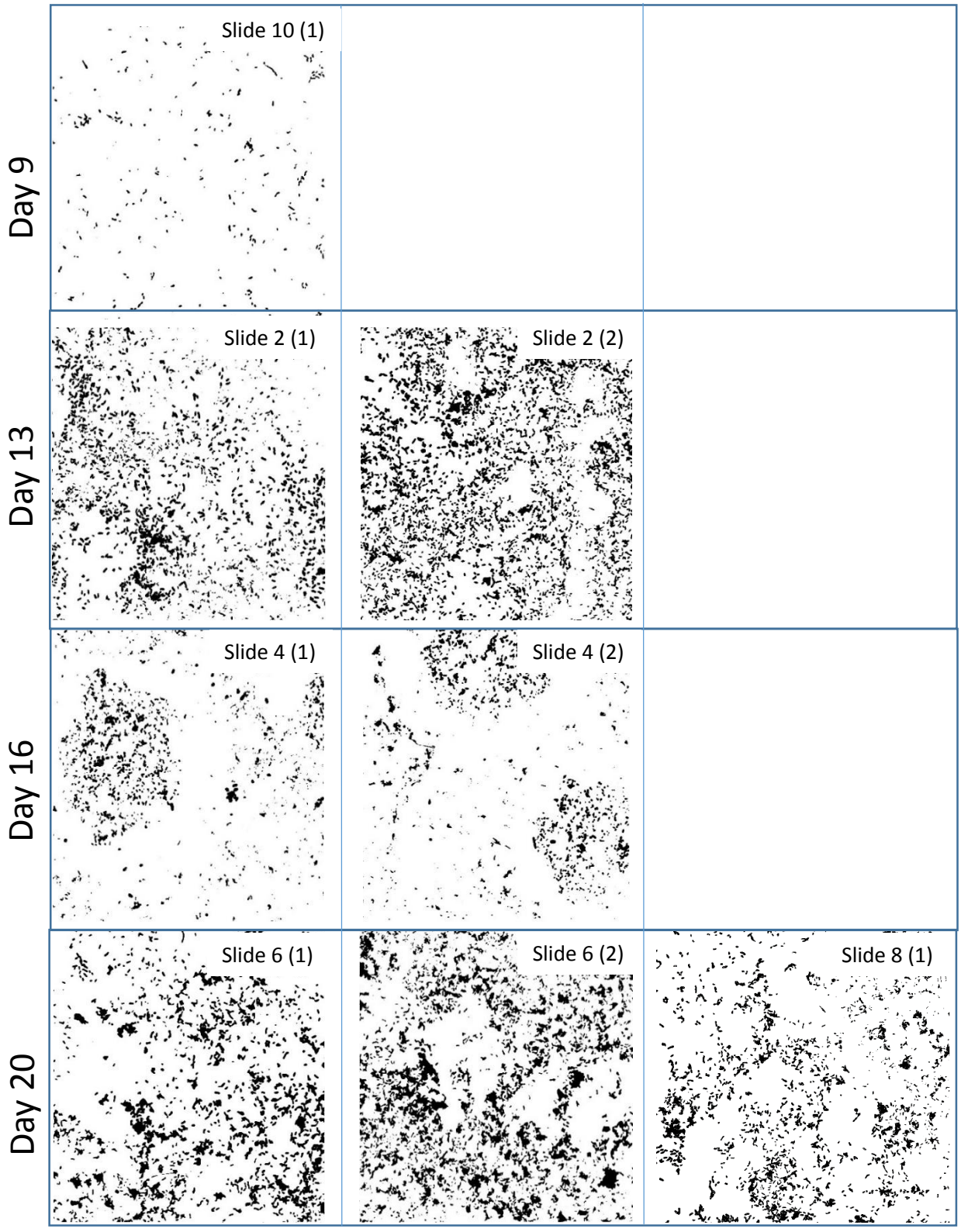

Table C.1. IMARIS Data from confocal image files.

		Volume (µm3)	Cell Count
Slide 3 - Day 9	Image 1	110.59	5.49E+07
	Image 2	169.11	8.39E+07
	Image 3	159.18	7.90E+07
	Image 4	159.34	7.91E+07
	Image 5	231.83	1.15E+08
	Image 6	104.4	5.18E+07
	Average	155.74	**7.73E+07**
	Std. Dev.	42.17	**2.09E+07**
Slide 10 - Day 11	Image 1	1645.6	8.17E+08
	Image 2	1796.45	8.92E+08
	Image 3	2613.84	1.30E+09
	Image 4	1519.58	7.54E+08
	Image 5	1712.77	8.50E+08
	Image 6	3652.5	1.81E+09
	Average	2156.79	**1.07E+09**
	Std. Dev.	757.23	**3.76E+08**
Slide 9 - Day 12	Image 1	1166.94	5.79E+08
	Image 2	844.63	4.19E+08
	Image 3	742.89	3.69E+08
	Image 4	915.56	4.54E+08
	Image 5	925.26	4.59E+08
	Image 6	2222.46	1.10E+09
	Average	1136.29	**5.64E+08**
	Std. Dev.	502.29	**2.49E+08**
Slide 4 - Day 13	Image 1	2726.22	1.35E+09
	Image 2	2067.55	1.03E+09
	Image 3	2067.55	1.03E+09
	Image 4	1737.44	8.62E+08
	Image 5	2410.07	1.20E+09
	Image 6	1339.77	6.65E+08
	Average	2058.1	**1.02E+09**
	Std. Dev.	445.21	**2.21E+08**

Table C.1. (Continued) IMARIS Data from confocal image files.

		Volume (µm3)	Cell Count
Slide 5 - Day 15	Image 1	2676.14	1.33E+09
	Image 2	2261.79	1.12E+09
	Image 3	2454.86	1.22E+09
	Image 4	2213.94	1.10E+09
	Image 5	2678.37	1.33E+09
	Image 6	1953.61	9.70E+08
	Average	2373.12	**1.18E+09**
	Std. Dev.	259.94	**1.29E+08**
Slide 8 - Day 17	Image 1	2023.38	1.00E+09
	Image 2	2681.18	1.33E+09
	Image 3	1400.39	6.95E+08
	Image 4	1967.14	9.76E+08
	Image 5	1953.72	9.70E+08
	Image 6	964.86	4.79E+08
	Average	1831.78	**9.09E+08**
	Std. Dev.	536.82	**2.66E+08**
Slide 7 - Day 19	Image 1	3297.21	1.64E+09
	Image 2	3506.93	1.74E+09
	Image 3	2744.25	1.36E+09
	Image 4	3017.36	1.50E+09
	Image 5	2732.34	1.36E+09
	Image 6	3074.3	1.53E+09
	Average	3062.07	**1.52E+09**
	Std. Dev.	278.41	**1.38E+08**

APPENDIX D: CALCULATIONS

Calculation D.1. Proof Acetate Never Limiting

Time acetate is in contact with MnO_2: Determine flow velocity through cylinder reactor at each flow rate over length of slides (3"=7.62cm) and calculate length of time the reaction is occurring.

Flow Rate: 5 mL/hr

$$\frac{7.62\ cm}{\frac{5\ mL}{hr}*\frac{1\ cm^3}{1\ mL}*\frac{1}{\pi*\left(\frac{3.49cm}{2}\right)^2}} = 14.58\ hr$$

Flow Rate: 50 mL/hr

$$\frac{7.62\ cm}{\frac{1.5\ mL}{hr}*\frac{1\ cm^3}{1\ mL}*\frac{1}{\pi*\left(\frac{3.49cm}{2}\right)^2}} = 1.45\ hr$$

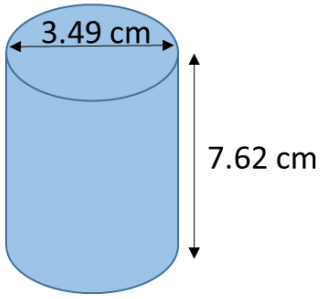

Acetate concentration in Effluent: Use the time acetate is in contact with MnO_2 to determine acetate utilized over the course of the reaction and subtract this from the initial acetate (1 mmol) to estimate effluent acetate concentration. (Maximum slope from fourth experiment used, see Table 1 in Results.)

Flow Rate: 5 mL/hr

$$Acetate\ Used\ Per\ Hour = \frac{1\ mmol\ Ac}{4\ mmol\ Mn} * \frac{2.28x10^{-2}\ mmol\ Mn}{day} * \frac{1\ day}{24\ hr} = \frac{2.38x10^{-4}\ mmol\ Ac}{hr}$$

$$Acetate\ in\ Effluent = 1\ mmol - \frac{2.38x10^{-4}\ mmol\ Ac}{hr} * 14.58\ hr = 0.996\ mmol$$

Flow Rate: 50 mL/hr

$$Acetate\ in\ Effluent = 1\ mmol - \frac{2.38x10^{-4}\ mmol\ Ac}{hr} * 1.46hr = 0.999\ mmol$$

Calculation D.2. Characteristic times of advection, diffusion, and reaction

Advection: $\tau_{adv} = \frac{length}{velocity} = \frac{7.62\ cm}{1.5x10^{-6}\frac{m}{s}*\frac{100\ cm}{1\ m}} * \frac{1\ min}{60\ s} * \frac{1\ hr}{60\ min} \approx 14\ hrs$

The advection length scale was assumed to be the length of one slide, and the velocity was taken as the average linear velocity.

Diffusion: $\tau_{diff} = \frac{length^2}{Diffusion} = \frac{\left(\mathbf{0.21\ cm}*\frac{\mathbf{10{,}000\ \mu m}}{\mathbf{1\ cm}}\right)^2}{\mathbf{3.12x10^6}\frac{\mu m^2}{hr}} \approx 1.4\ hr$

The diffusion length scale was assumed to be half of the distance between two slides (0.21 cm), and the diffusion is the diffusion of acetate in water.

Reaction: $\tau_{rxn} = \left(\frac{Y}{\mu_{max}}\right)\left(\frac{k_{MN}+Mn}{B}\right) = \left(\frac{3.44x10^{10}\frac{cells}{mmol\ MnO_2}}{0.02\ \frac{1}{hr}}\right)\left(\frac{0.04\ mmol\ MnO_2+0}{1x10^9\ cells}\right) \approx 69\ hr$

The yield, maximum specific growth rate, and half saturation constant were determined from experimental data. The mass of Mn was chosen to be zero in order to estimate the shortest possible characteristic time. And 1x10^9 cells was used for the biomass because approximately this amount of biomass was determined at late times for the experiments.

** The reaction characteristic time is considerably longer than diffusion and advection, and this is also expected at higher flow rates, as the velocity will be higher, making τ_{adv} even smaller.

Calculation D.3. Estimate initial manganese mass example

Slide mass (m_s): 4.4947 g

Slide mass after coating with MnO_2 (m_{sc}): 4.5002 g

Molar mass of manganese dioxide: 86.94 g/mol

$$Mn_0 = \frac{m_{sc} - m_s}{MM_{MnO_2}} * \frac{1\ mol\ Mn}{1\ mol\ MnO_2} = \frac{4.5002g - 4.4947g}{86.94\frac{g}{mol}MnO_2} * \frac{1\ mol\ Mn}{1\ mol\ MnO_2} = 6.33x10^{-5}\ mol\ Mn$$

Calculation D.4. Derive Analytical Solution

$$\frac{d[MnO_2]}{dt} = -A * \left(\frac{[MnO_2]}{k_{MN} + [MnO_2]}\right)$$

$$\int_{Mn_0}^{Mn} \frac{k_{MN} + [MnO_2]}{[MnO_2]} d[MnO_2] = \int_0^t -A * t$$

$$\int_{Mn_0}^{Mn} \frac{k_{MN}}{[MnO_2]} d[MnO_2] + \int_{Mn_0}^{Mn} 1 * d[MnO_2] = -A * t$$

$$k_{MN} * \log(\mathrm{Mn}) - k_{MN} * \log(Mn_0) + Mn - Mn_0 = -A * t$$

$$A * t = k_{MN} * \log\left(\frac{Mn_0}{Mn}\right) - Mn + Mn_0$$

Calculation D.5. Calculate Literature Yield from Thermodynamics (Roden & Jin, 2011)

$$CH_3COO^- + 8H^+ + 4MnO_{2\,(s)} \rightarrow HCO_3^- + CO_2 + 4Mn^{2+} + 5H_2O$$

ΔG = -563.93 kJ/mol Acetate

$$Y = 2.08 + 0.0211 * \left(563.93 \frac{kJ}{mol\ Ac}\right) = \frac{13.98\ g\ cells}{mol\ Ac}$$

$$Y = \frac{13.98\ g\ cells}{mol\ Ac} * \frac{1\ mol}{1000\ mmol} * \frac{Geobacter\ cell}{2x10^{-13} g} * \frac{1\ mol\ Ac}{4\ mol\ MnO_2}$$

$$Y = 1.75x10^{10} \frac{cells}{mmol\ MnO_2}$$

APPENDIX E: MODEL OUTPUTS

Figure E.1. Changing Biomass Model behavior to changes in parameters.

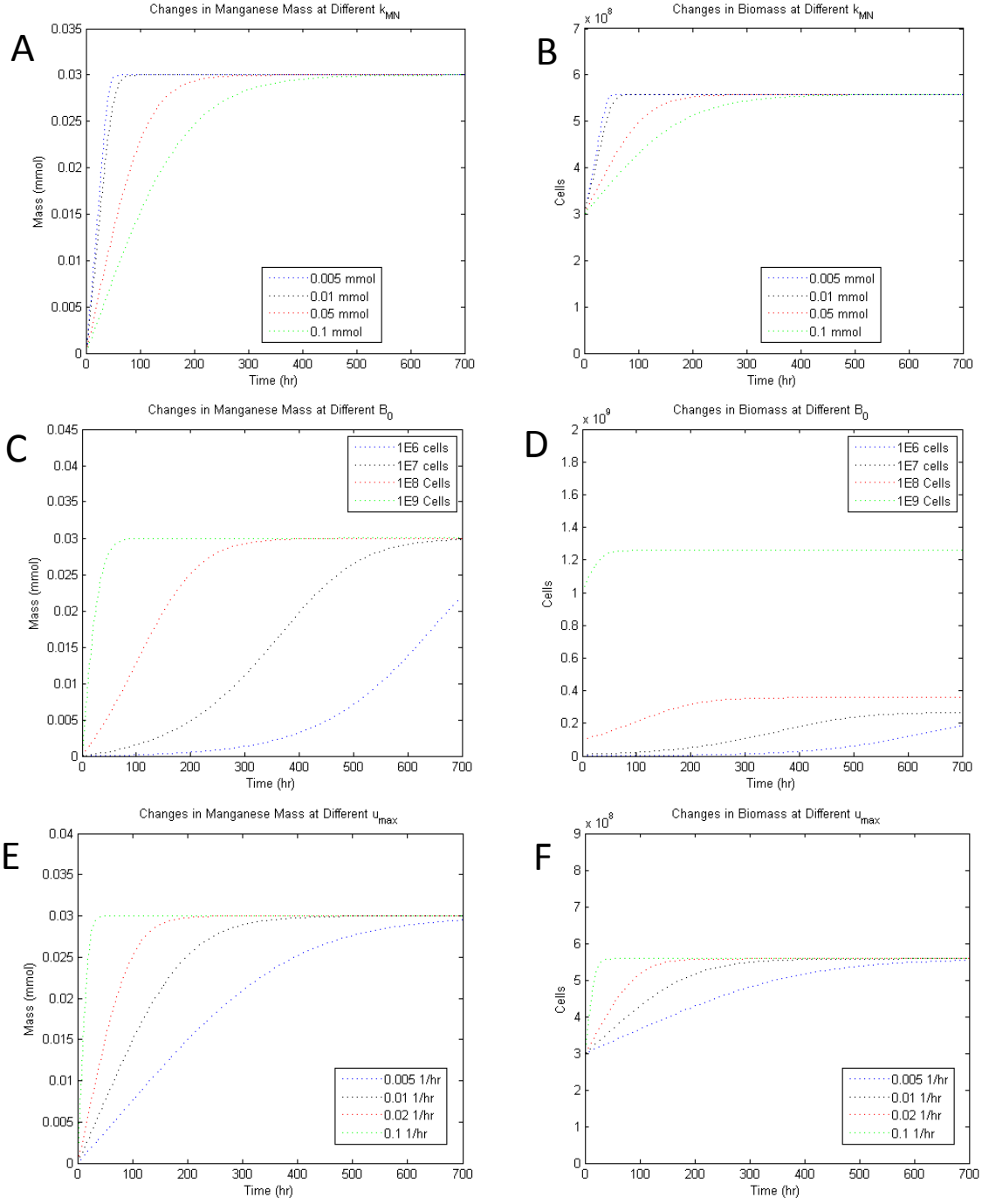

Figure E.1. (Continued) Changing Biomass Model behavior to changes in parameters.

G

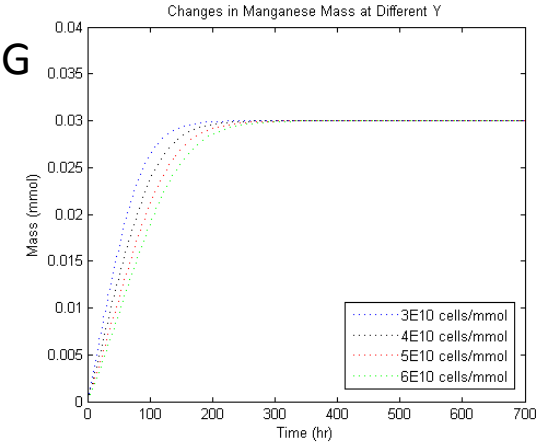

H

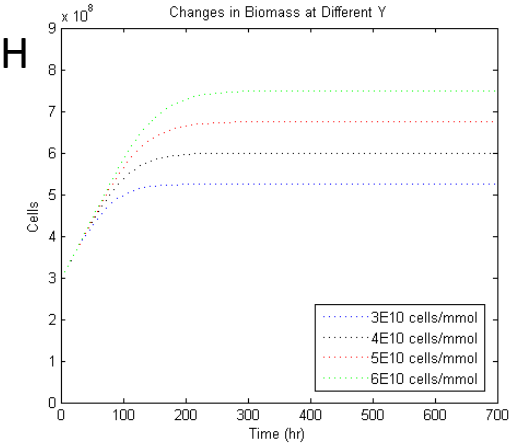

I

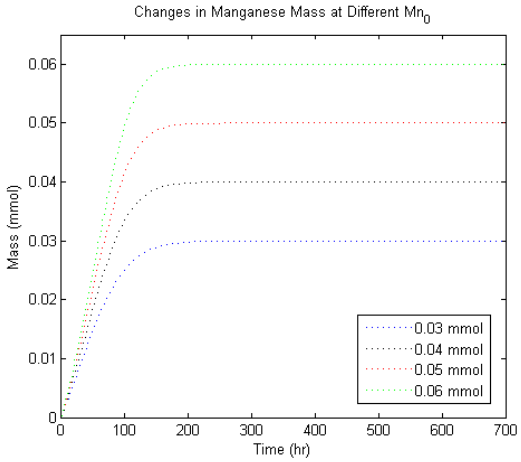

J